

Politecnico di Torino

Master's degree in Automotive Engineering

Battery SoH Estimation Through Non-Destructive Methods

Academic Supervisor: Candidate: Ezio Spessa Antonio Maria Mancino

Academic year 2024/2025

Abstract

The growing proliferation of electric and hybrid vehicles in recent years has led to a rapid and significant acceleration in the evolution of energy storage technologies. This, in turn, has generated an increasingly pressing need to monitor the health status of battery cells with precision, consistency, and standardization, especially now that the second-hand market for such vehicles is steadily expanding, along with the amount and variety of data that can be acquired from batteries used in diverse operating conditions.

This thesis stems from the need to develop a standardized and easily reproducible diagnostic system for assessing battery health in the automotive sector. The focus of the study is on the Electrochemical Impedance Spectroscopy (EIS) procedure. The initial goal was to infer the State of Health (SoH) of the batteries through impedance measurements at specific frequencies. However, as the study progressed, it became increasingly evident that this methodology holds a broader potential, capable of providing a more comprehensive representation of the battery health state.

The analysis begins with a critical review of the existing non-destructive diagnostic techniques for batteries, explaining the methodological choices adopted. Once the diagnostic approach was selected and the theoretical analysis completed, the experimental procedure is presented in detail, it consisted in controlled laboratory measurements conducted on cylindrical batteries 18650 typically used in domestic applications, allowing the collection of data that were both repeatable and interpretable. The development of an equivalent circuit model, together with a dedicated code capable of representing the data in a useful and meaningful way, enabled comparison with real-world data and the extraction of valuable insights from them.

Finally, the thesis discusses the prospects for industrialization, highlighting the remaining challenges in terms of miniaturization, signal robustness in noisy environments, and the inherent difficulty of conducting a large-scale data collection campaign.

1.	INT	TRODUCTION	7
	1.1.	Approach	9
2.	SOI	1 AND SOC	10
	2.1.	STATE OF CHARGE (SOC)	10
	2.2.	SoH estimation methods	
	2.3.	COULOMB COUNTING	11
	2.4.	OPEN CIRCUIT VOLTAGE (OCV)	12
	2.5.	KALMANN FILTER	13
	2.6.	ELECTROCHEMICAL IMPEDANCE SPECTROSCOPY (EIS)	14
	2.7.	CONCLUSIONS	15
3.	TH	EORETICAL BACKGROUND FOR ELECTROCHEMICAL IMPEDANCE SPECTROSCOPY	16
	3.1.	ALTERNATING CURRENT AND SINUSOIDAL PERTURBATIONS	16
	3.2.	COMPLEX NUMBERS IN AC ANALYSIS	
	3.3.	IMPEDANCE OF IDEAL ELEMENTS	
	3.4.	IMPEDANCE OF ELECTROCHEMICAL SYSTEMS	
	3.5.	NYQUIST AND BODE REPRESENTATIONS	
	3.6.	BATTERY STATE DURING MEASUREMENT	18
4.	AR	FIFICIAL AGING OF LITHIUM-ION BATTERIES	21
	4.1.	BATTERY AGING MECHANISMS	21
	4.2.	FACTORS ACCELERATING BATTERY AGING	21
	4.3.	ARTIFICIAL AGING PROTOCOL	
	4.3.	1. Initial Characterization	22
	4.3.		
	4.3.	F	
	4.3.		
	4.3.	0 0	
	4.3.		
	4.3.		
5.		PERIMENTAL SETUP AND METHODOLOGY	
		MEASUREMENT ARCHITECTURE	
	5.2.	AUXILIARY EQUIPMENT AND CONDITIONING	
	5.3.	TEMPERATURE CONTROL AND MONITORING	
	5.4.	ELECTRICAL CONNECTIONS AND MECHANICAL STABILITY	
	5.5.	CALIBRATION AND VERIFICATION PROCEDURES	
	5.6. 5.7.	MITIGATION OF MEASUREMENT ARTIFACTS	
	5.7. 5.8.	DATA HANDLING AND TRACEABILITY OVERVIEW	
	5.6. 5.9.	EXPERIMENTAL CHALLENGES AND ITERATIVE IMPROVEMENTS	
	5.10.	OPTIMIZATION OF THE CONTACT INTERFACE	
	5.11.	CONTROL OF ELECTROCHEMICAL CONDITIONING	
	5.12.	CALIBRATION FREQUENCY AND REFERENCE VALIDATION	
	5.13.	REPEATABILITY ASSESSMENT	
	5.14.	CONSOLIDATION OF BEST PRACTICES	
	5.15.	PRELIMINARY DATA VALIDATION AND QUALITY ASSESSMENT	
	5.16.	DATA SCREENING CRITERIA	
	5.17.	OBSERVATIONS AND INCREMENTAL REFINEMENTS	
	5.18.	SUMMARY OF EXPERIMENTAL RELIABILITY	
	5.19.	RESIDUAL LIMITATIONS AND PRACTICAL CONSIDERATIONS	

	5.20.	DATA ROBUSTNESS AND REPRODUCIBILITY	32
	5.21.	LESSONS FROM THE EXPERIMENTAL CAMPAIGN	32
6.	PH	SICAL PRINCIPLES OF DEGRADATION IN LITHIUM-ION BATTERIES	33
	6.1.	Overview: what really "ages"	33
	6.2.	INTERFACES AND LAYERS: SEI AND CEI	33
	6.2.	1. SEI on the anode (Graphite/Silicon)	33
	6.2	2. CEI on the cathode	34
	6.3.	LITHIUM PLATING	34
	6.4.	CATHODE DEGRADATION: CHEMISTRY, STRUCTURES, AND TRANSITION METALS	35
	6.4.	1. Dissolution of transition metals	35
	6.4	2. Oxygen release and phase transitions	35
	6.4	3. Cracking from "lattice breathing"	35
	6.5.	ELECTROLYTE AND CONDUCTIVE SALT: BASIC CHEMISTRY	35
	6.6.	MECHANICS AND PERCOLATION: WHEN THE STRUCTURE BREAKS DOWN	36
	6.7.	EXTREME EVENTS: OVER-DISCHARGE, OVER-CHARGE, AND SAFETY	36
	6.8.	MAP OF OPERATING CONDITIONS	
	6.9.	INTERNAL HETEROGENEITY AND "UNEVEN AGING"	
	6.10.	MACROSCOPIC OBSERVATIONS AND "SIGNATURES" OF MECHANISMS	
	6.11.	Engineering and control implications	
	6.12.	OPERATIVE SUMMARY	
	6.13.	Transition towards model representation	38
	6.13	, ,	
	6.13		
	6.13	3.3. Cracking and loss of percolation (LAM)	39
	6.13	3.4. Cathode effects and dissolution of transition metals	39
	6.13	,,	
	6.13	,,	
	6.13	Phenomenological synthesis	40
7.	EQU	JIVALENT CIRCUIT MODEL FOR AGEING PHENOMENA IN LITHIUM-ION BATTERIES	42
	7.1	Introduction	42
	7.2	MODELING USING EQUIVALENT CIRCUITS	42
	7.3	FROM EXPERIMENTAL MEASUREMENT TO ANALYTICAL MODEL	42
	7.4	PHYSICAL MEANING OF PARAMETERS	43
	7.5	CORRELATION BETWEEN ELECTRICAL PARAMETERS AND AGING PHENOMENA	44
	7.6	PRACTICAL UTILITY OF MODELING	44
	7.7	COMBINATION OF MULTIPLE PROCESSES	45
	7.8	DIFFUSION EFFECTS AND NON-IDEAL BEHAVIOR	46
	7.9	STIMA DEI PARAMETRI E CONFRONTO CON I DATI SPERIMENTALI	46
	7.10	PARAMETRIC VARIATION AND PREDICTIVE SIMULATION	48
	7.11	SENSITIVITY ANALYSIS OF PARAMETERS	49
	7.12	DYNAMIC IDENTIFICATION AND FITTING STABILITY	49
	7.13	COMPARATIVE ANALYSIS OF THE MODELS CONSIDERED	50
	7.14	CHOICE OF MODEL ADOPTED	51
	7.15	ROBUST IDENTIFICATION STRATEGIES	52
	7.16	SUMMARY AND IMPLICATIONS	55
8.	ANA	ALYSIS OF FITTING RESULTS AND CORRELATION WITH HEALTH STATUS	56
	8.1	FITTING PROCEDURE	
	8.2	PHYSICAL CONSISTENCY AND INTERPRETATION OF RESULTS	
	8.3	GRAPHICAL REPRESENTATION AND COMPARISON OF CONDITIONS	
	0.0	GAGA AAAAA INDI INDODII III IOO III IOO OOFII III II OOTI OOT	

8.4	EVOLUTION OF PARAMETERS AND CORRELATION WITH SOH	58
8.5	Conclusions	59
o. IN	regration of the model into the diagnostic and predictive context	60
9.1.	FROM THE FREQUENCY DOMAIN TO THE TIME DOMAIN	60
9.2.	MODELLING OF THE PARAMETRIC EVOLUTION	60
9.3.	IDENTIFICATION AND TRACKING OF THE AGEING PHENOMENA	61
9.4.	TOWARDS AN ADAPTIVE AND PREDICTIVE MODEL	62
9.5.	Conclusions	62
IBLIO	GRAPHY	64

Figure 1: Electric and hybrid vehicle sales comparison to the entire car fleet	7
Figure 2: Number of vehicles sales in absolute terms per year.	8
Figure 3: compact vehicle ICEV and an equivalent BEV cost subdivision	9
Figure 4: Visual representation of SoC and SoH	11
Figure 5: first measurement attempt layout	27
Figure 6: battery holder	28
Figure 7: SEI formation	34
Figure 8: Lithium plating process	34
Figure 9: comparison between direct and derived data	47
Figure 10: close up on comparison between direct and derived data	48
Figure 11: degraded battery Nyquist plot	58

1. Introduction

The objective of this thesis arises from the need to evaluate the **State of Health (SoH)** of lithium batteries, typical of modern electric cars. Therefore, it will be analyzed where this necessity comes from and why it is likely to become increasingly urgent in the next years to come.

It Is beyond doubt that the world of automotive finds itself in a pivotal moment. The European Union's restrictions on internal combustion vehicles and public awareness on environmental issues, alongside the maturity of propulsion technologies, have led to a sudden increase in the demand for electric vehicles.

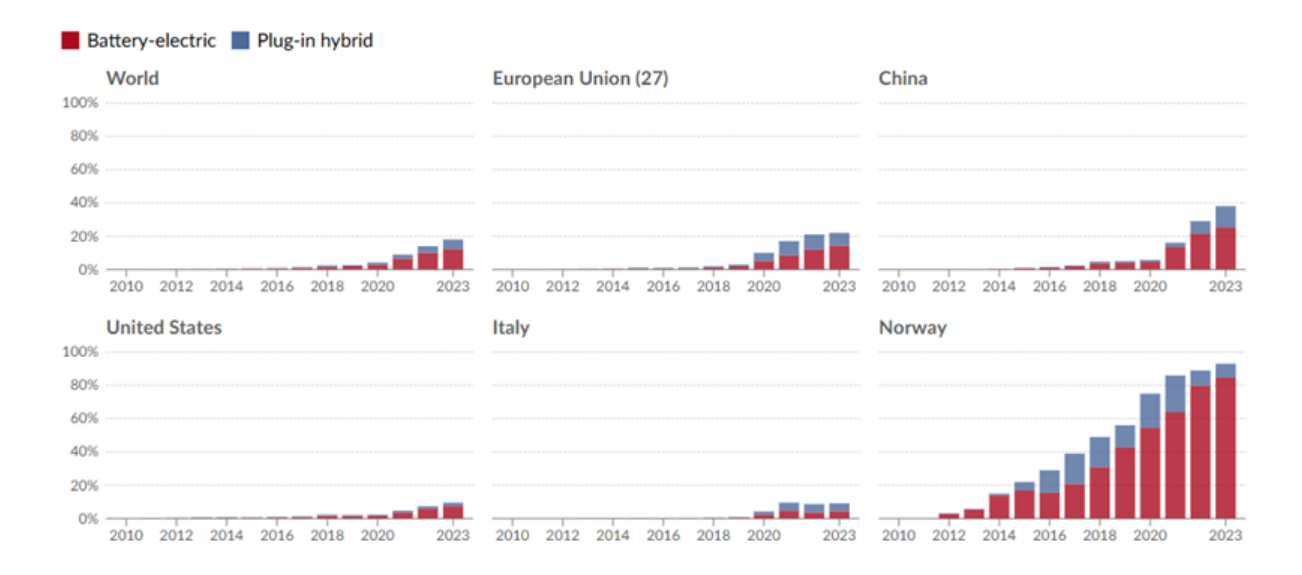


Figure 1: Electric and hybrid vehicle sales comparison to the entire car fleet.

In this thesis, plug-in hybrid vehicles will be included as well alongside electric cars. This choice stems from the fact that this study is to evaluate the impact of lithium batteries as a component of the car of tomorrow, which plays a key role in both architectures.

Introduction

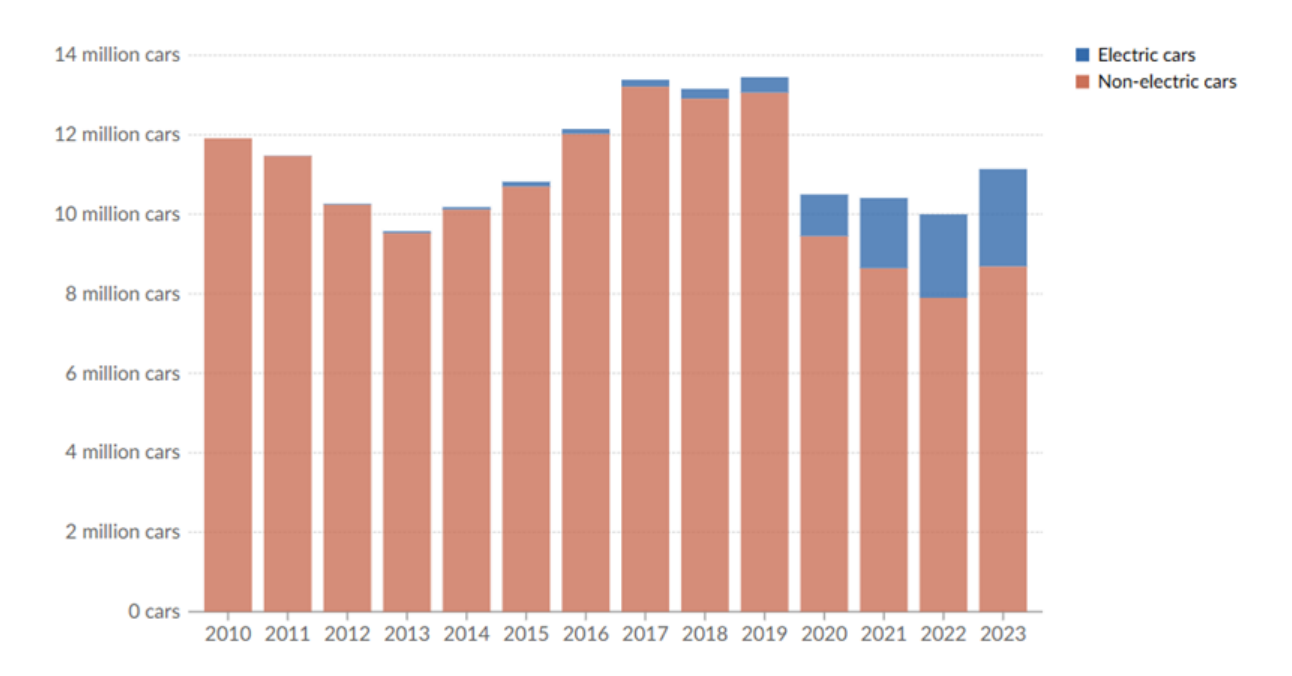


Figure 2: Number of vehicles sales in absolute terms per year.

Assessing the number of vehicle sales in absolute terms allows us to realize how complex the situation is and leaves us room for different interpretations. First of all, it is evident that in recent years there has been a drastic drop in sales of electric and hybrid vehicles. However, this drop is smaller in percentage terms than the general slowdown in sales of private vehicles. This resulted in a percentage increase as shown in Figure 1.1. Hybrid vehicles show an even more pronounced upward trend since the collapse in sales in 2020. In short, in light of this data, it appears to be difficult to make reliable predictions about the future of the market. On the other hand, it is possible to say with sufficient certainty that electric vehicles have already established themselves on the global transport scene and it would not be surprising to see their numbers increase in line with further technological advances.

Another factor that highlights the growing importance of batteries in this sector is their cost and the projected future value of this cost in relation to the total cost of the vehicle.

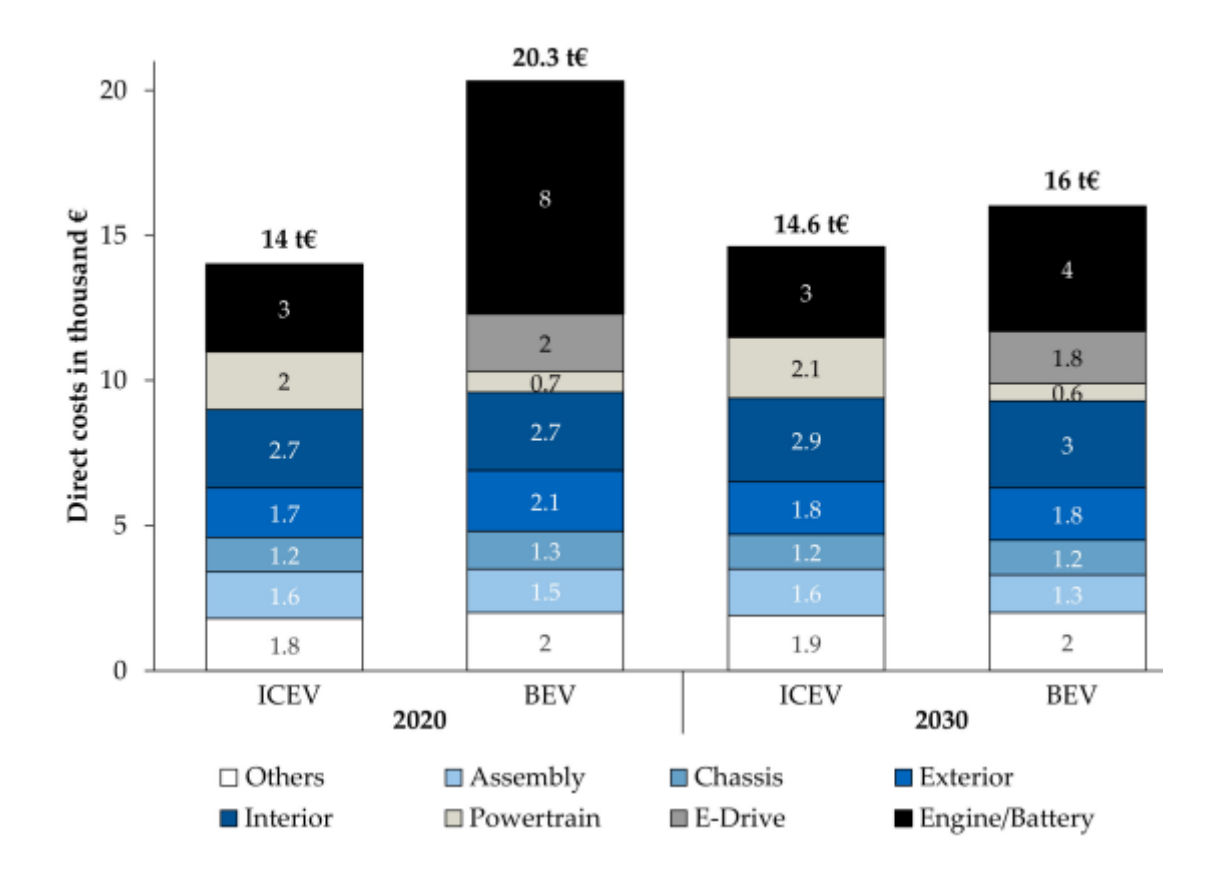


Figure 3: compact vehicle ICEV and an equivalent BEV cost subdivision

As we can see in the graph in Figure 1.3, it is possible to observe how the price of the battery in 2020 used to represent one third of the entire cost of the vehicle, while lower values are projected as the technology matures. However, it still remains the most expensive component of the vehicle.

It is therefore obvious how the assessment of the State of Health of the battery of an electric vehicle represents an increasingly important process, n ot only from a collective point of view due to the increase of the number of electric vehicles but also from the individual user standpoint individual user, since the assessment of this component represents an estimate of the condition of the most expensive component of the car.

1.1. Approach

In battery management systems, it is possible to identify two key parameters that play a crucial role in assessing battery performance and reliability: **State of Health (SoH)** and **State of Charge (SoC)**. These two metrics provide valuable insights into the battery's condition and its ability to store and deliver energy efficiently over time.

2. SoH and SoC

The **State of Health** is one of the indicators used to assess a battery's overall condition relative to its new and unused initial state. This metric reflects the degree of aging and degradation the battery has undergone and is typically expressed as a percentage. Here, **100%** represents a new battery, and lower values indicate a progressive wear.

With time, batteries experience **capacity to fade**, meaning they gradually lose the ability to store the same amount of charge as when they were first manufactured. Moreover, their **internal resistance increases**, which leads to higher energy losses and reduced efficiency. These factors, along with changes in voltage response and self-discharge rates, contribute to the overall decline in the SoH of the battery.

Various methodologies have been developed in the past years in order to estimate SoH. These methodologies include open circuit voltage (OCV) analysis, electrochemical impedance spectroscopy (EIS) and incremental capacity (IC) analysis. Machine learning models are increasingly being used to analyze large datasets and can predict battery health with very high accuracy. Even though these approaches can differ in complexity and precision, their common goal is to provide a reliable assessment that is able to provide a clear picture of a battery's remaining useful life. This assessment serves to determine whether the battery should be reused, repurposed, or recycled.

2.1. State of Charge (SoC)

While SoH provides a long-term perspective on battery degradation, the **State of Charge** (SoC) represents a battery's real-time charge level. SoC indicates how much energy is available at any given moment, making it a critical parameter for energy management in applications such as **electric vehicles (EVs) and renewable energy storage**.

Unlike SoH, which can change gradually over months or years, SoC fluctuates depending on charging and discharging events in a dynamic way. There are many different methods that can estimate SoC. They include **open circuit voltage measurement**, Coulomb counting, and Kalman filtering techniques.

2.2 The Relationship Between SoH and SoC

Although SoH and SoC serve different purposes, they are closely interconnected. A battery with a lower SoH will exhibit a reduced capacity, meaning that even if its SoC is 100%, the actual energy that is able to deliver will be lower than that of a new battery. This relationship is important in energy-intensive applications, as accurate SoC estimation must account for degradation over time.

What is essential for optimizing battery performance, extending lifespan, and ensuring safe operation is having a clear understanding of both SoH and SoC. As battery technology

advances, more sophisticated estimation methods continue to emerge. These methods are crucial to helping improve the reliability and efficiency of modern energy storage systems.

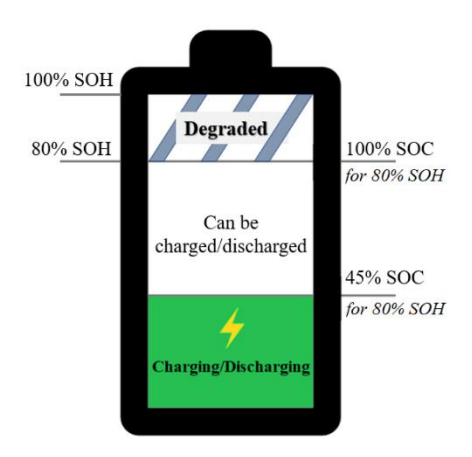


Figure 4: Visual representation of SoC and SoH

2.2. SoH estimation methods

We are going now to describe the main methods that have been taken into consideration for our analysis, based on the available literature.

2.3. Coulomb counting

In order to assess a battery State of Health, a technique that is widely used is Coloumb counting. This process follows two main steps. The first one, the total discharged capacity, Q_discharge, is determined by integrating the discharge current over time until the State of Charge (SoC) reaches 0%. Then the SoH is estimated by comparing this discharged capacity with the battery's rated capacity, using the following relationship:

$$Q_{discharge} = \int_0^T I(t)dt \ SoH(\%) = \frac{Q_{discharge}}{Q_{rated}} \times 100$$

To apply this method, key battery parameters must be continuously monitored. Such parameters include charge/discharge current, voltage, and temperature. An adaptive approach can also be implemented by recalculating SoH during each discharge cycle. Studies have demonstrated that Q_discharge decreases as the number of charge/discharge cycles increases, leading to a gradual decline in SoH. In general, we can see that when SoH drops below 80%, the battery is considered to have reached the end of its useful life. The accuracy of this method depends heavily on precise current measurements, which makes periodic calibration of sensors essential.

Another crucial factor that influences Coulomb counting's reliability is the accuracy of the initial SoC estimation. The **Depth of Discharge (DoD)** metric is introduced in order to better characterize this discharge process. DoD follows a very similar principle to SoC:

$$DoD = \frac{Q_{released}}{Q_{rated}} \times 100$$

where **Q_released** represents the total capacity discharged from the battery. At any given moment, DoD can be expressed as:

$$DoD(t) = DoD(t_0) + \eta \cdot \Delta DoD$$

$$\Delta DoD = \int_{t_0}^{t_0 + \tau} I_b(t) dt \div Q_{rated} \times 100$$

where I_b is the battery's charge/discharge current and η represents the system's efficiency. Then, SoH is determined by tracking the DoD when the battery reaches its fully discharged state. The charge/discharge efficiency is factored into each cycle to maintain accuracy, and recalibration occurs at both the fully charged and fully discharged states.

This is usually the preferred method because of its low implementation cost, minimal computational requirements, and easily integration into Battery Management Systems (BMS). However, its accuracy improves over multiple charge/discharge cycles, with errors as low as 1% after 28 cycles.

2.4. Open circuit voltage (OCV)

The State of Health of batteries is done by establishing a functional relationship between the SoH and the OCV of the monitored battery. This technique can be implemented in offline and online configurations. They both present distinct advantages and limitations.

The fundamental principle of the OCV method relies on a simplified electrical model of the battery, where the OCV is expressed as:

$$U_{OCV} = U + IR$$

where Uocv represents the battery's open-circuit voltage, I is the current, R denotes the internal resistance and is the terminal voltage of the battery. Thanks to this equation, it becomes possible to correlate the OCV with the SoH under controlled conditions.

The offline approach requires extensive laboratory testing to establish OCV curves that correspond directly to various states of health. These tests involve measuring the OCV at different states of charge while also considering external influences such as temperature variations. Research has demonstrated that temperature significantly affects the accuracy of OCV-SoC curves. Therefore, proper compensation techniques must be employed when high-precision SoH estimation is required. Despite its reliability, the offline approach necessitates an extensive amount of data collection and experimental validation, eventually making this approach costly and time-consuming.

On the other hand, the online implementation of the OCV method involves incorporating OCV as a parameter within an electrical model and estimating its value through system identification techniques. Factors such as initial SoC assumptions and temperature fluctuations can influence the accuracy of this method. A key challenge in this type of approach is making sure that the assumed initial SoC aligns well with the actual SoC in order to minimize estimation errors. Studies have reported that lower battery temperatures tend to introduce root-mean-square errors (RMSE) in the range of 5% to 25%, affecting the overall accuracy of SoH predictions.

Furthermore, several studies have explored different methodologies that are able to enhance the accuracy and practicality of OCV-based SoH estimation. One approach involves integrating OCV with other modeling techniques, which helps refine estimations. For example, research has demonstrated that using OCV alongside an electrical battery model improves accuracy while reducing dependency on empirical OCV-SoC curves. Some studies have investigated the combination of OCV with Coulomb counting, which allowed to reach a more robust SoH estimation framework that compensates for the limitations of individual methods.

Despite its clear effectiveness, certain challenges limit the practical application of OCV for real-time SoH estimation. One major drawback is that OCV is difficult to measure in an accurate way in operational conditions, as it requires the battery to be in a relaxed state without any charge or discharge activity. Some researchers have proposed utilizing alternative model-based approaches that approximate SoH more efficiently while reducing computational and hardware requirements, which ultimately leads to eliminating direct reliance on OCV.

Recent advancements have also investigated the fusion of OCV estimation with data-driven techniques, which include machine learning algorithms to improve predictive accuracy. Hybrid models that integrate OCV with incremental capacity (IC) analysis or other statistical methods have demonstrated promising results such as achieving estimation errors as low as 1% in certain cases.

Overall, the OCV-based method remains a fundamental approach to SoH estimation. This is thanks to its simplicity and effectiveness in controlled environments. However, its limitations in practical applications call for the integration of complementary methods which will finally enhance accuracy, reliability, and real-time applicability.

2.5. Kalmann Filter

The Kalman Filter is a commonly used method for estimating the states of a dynamic system. It operates in two main phases: the prediction phase and the update phase. During the prediction phase, the system's state is estimated based on prior knowledge and process dynamics. In the update phase, the filter incorporates new measurements, which are typically affected by Gaussian noise, to refine the state estimation. The standard Kalman filter equations define this recursive process, involving parameters such as the state transition matrix, control matrix, and measurement noise covariance.

Even though it was initially developed for linear systems, the Kalman filter has been adapted to nonlinear applications, such as battery State of Health estimation. In these cases, modified versions of the Kalman filter are often employed, including the Extended Kalman Filter (EKF) and the Unscented Kalman Filter (UKF). The EKF extends the standard Kalman filter to nonlinear systems by linearizing the transition and measurement equations. It is useful in the SoH estimation when it is paired with a battery electrical model, as the Randles circuit model. A dual EKF approach has been proposed in which two separate Kalman filters run in parallel: one for estimating the State of Charge and another for tracking the battery's capacity.

The UKF, also known as the Sigma Point Kalman Filter (SPKF), addresses some of the limitations of the EKF. The UKF represents the state distribution using a set of sigma points that better capture the nonlinear transformations instead of relying on linearization. Studies have shown that the UKF enhances the SoH estimation accuracy by handling process nonlinearities in an effective way. In comparative evaluations, the UKF demonstrates lower estimation errors than traditional Coulomb counting methods, with error margins below 3%.

The Kalman filter has been applied in conjunction with various battery models. For instance, some researchers have used a second-order Randles model to define the state equations for the EKF, estimating the SoH based on SoC or internal battery impedance. Other studies have proposed that using the UKF alongside machine learning techniques, such as Support Vector Regression (SVR), would be able to determine initial capacity values and enhance the SoH prediction accuracy. Furthermore, adaptive Kalman filtering techniques have been explored as well. They include methods aimed at updating lookup tables based on real-time battery conditions, which eventually improves the robustness of aging estimation models.

Despite its many advantages, the Kalman filter has been observed to have its limitations. For instance, the EKF is prone to divergence if the initial state is not defined properly, which leads to inaccuracies in the SoH estimation. Moreover, the approximation of posterior mean and covariance in nonlinear systems can introduce significant errors. The UKF can mitigate some of these challenges, but it requires more computational resources due to the increased number of sigma points.

Recent advancements have also included hybrid approaches, such as combining EKF with Quadratic Discriminant Analysis (QDA) for battery classification, or fusing Kalman filtering, with pattern recognition techniques. All these methods aim to refine the SoH estimation by leveraging model-based and data-driven approaches. Another new technique involves using the Kalman filter for continuous updates of battery resistance parameters, which requires dynamically adjusting the estimation model to real-time operating conditions.

Overall, the Kalman filter and its variants remain very powerful tools for the SoH estimation, offering a balance between accuracy and computational efficiency. However, ongoing research continues to refine these methods by working on integrating them with advanced modeling techniques and machine learning algorithms that would enhance their performance when used in practical applications.

2.6. Electrochemical Impedance Spectroscopy (EIS)

This methodology is based on the application of a current signal or low-amplitude alternating voltage, varying the frequency over a wide interval (typically from mHz to kHz) and on measuring the system response in terms of amplitude and phase shift.

The EIS data analysis is usually represented by Nyquist diagrams or Bode diagrams, in which the real and imaginary parts of the impedance provide us with information on the various physical and chemical phenomena that occur in the battery.

- **High-frequency region**: is dominated by total ohmic resistance, which includes electrolyte resistance, contacts, and connections.
- **Mid-frequency region**: is associated with charge transfer resistance and the formation or growth of the Solid Interfacial Layer (SEI).
- Low frequency region: is influenced by diffusion processes (Warburg impedance) and slow electrochemical kinetics.

In the context of the assessment of the State of Health, the EIS represents a very informative approach. This is due to the battery's ageing modifies in a meaningful way electric parameters, related to internal resistance and reaction kinetics. The SoH is defined as the ratio between the maximum residual capacity of the battery and the nominal design capacity. The degradation can be monitored through measurable changes in the impedance spectrum.

Compared to other SoH estimation methods (such as electrochemical model-based approaches, data-driven methods, or full charge/discharge testing), EIS has the following advantages:

- **Non-invasive**: it does not require complete charge/discharge cycles which reduces time and stress on the cell.
- **High sensitivity**: it can detect subtle variations related to the formation of resistive layers, loss of active material, or electrolyte degradation.
- ∉ **Direct correlation with physical phenomena**: it allows variations in impedance that are linked to specific degradation mechanisms.

2.7. Conclusions

In light of the data collected, it is possible to observe how every method of SoH assessment is the result of the compromise between accuracy of results and difficulty of collection of the necessary data. Analyzing the different methods for estimating the health status of lithium-ion batteries, it has been opted for the use of the electrochemical impedance spectroscopy since it allows for an easier evaluation of possible errors, unlike other methods that are more sensitive to perturbations. Considering the context of automotive in our use, the various limitations on the counter require a fast and robust method, characteristics that are typical of EIS.

Another interesting characteristic of this method is its adaptability. We can choose the number of the frequencies over which taking measurements and increasing the measurement spectrum; we can acquire further information on certain aspects of the battery's chemical state, allowing an eventual improvement of the analysis service based on available resources.

3. Theoretical Background for Electrochemical Impedance Spectroscopy

Before diving into the experimental methods and the detailed discussion of equivalent circuit models, it is essential to establish the fundamental concepts that underly the measurement and interpretation of Electrochemical Impedance Spectroscopy. This third chapter aims to provide the theoretical background necessary to understand the relationship between alternating current (AC) perturbations, complex-number representations, and the impedance response of electrochemical systems. These explanations are tailored to the application of EIS to lithium-ion batteries, even though the principles can be applied to any electrochemical system.

3.1. Alternating Current and Sinusoidal Perturbations

EIS relies on perturbing the system with a small AC signal and observing its response. Unlike direct current (DC) measurements, where the applied signal is constant over time, AC measurements involve time-varying voltages or currents, typically sinusoidal in form:

$$v(t) = V_0 \cdot \sin(\omega t)$$

or

$$i(t) = I_0 \cdot \sin(\omega t + \phi)$$

where:

- V_0 and I_0 are the signal amplitudes,
- $\omega = 2\pi f$ is the angular frequency in rad/s,
- ϕ is the phase shift between voltage and current.

In an ideal resistor, voltage and current are **in phase** ($\phi = 0^{\circ}$), while in capacitive or inductive elements they are **out of phase**. This phase relationship provides valuable information about the system's internal processes.

In EIS, the perturbation amplitude is chosen to be small (typically 5–10 mV) so that the system remains within the **linear response regime**. This ensures that the impedance measured is independent of the amplitude and that the resulting data can be interpreted with linear-system theory.

3.2. Complex Numbers in AC Analysis

The use of sinusoidal signals introduces the need for a mathematical representation that can simultaneously capture magnitude and phase. This is where **complex numbers** become indispensable. Using Euler's formula:

$$e^{j\theta} = \cos\theta + j\sin\theta$$

we can express a sinusoidal signal as a complex exponential:

Theoretical Background for Electrochemical Impedance Spectroscopy

$$v(t) = \Re\{V_0 e^{j\omega t}\} i(t) = \Re\{I_0 e^{j(\omega t + \phi)}\}\$$

Here, j is the imaginary unit ($j^2 = -1$), and the quantities V_0 and I_0 can be expressed as **phasors**, which are complex numbers encoding at the same time amplitude and phase. This formalism allows algebraic manipulation of AC signals without the need to separately track sine and cosine components.

The impedance Z of a system is the ratio of the voltage phasor to the current phasor:

$$Z(\omega) = \frac{\tilde{V}(\omega)}{\tilde{I}(\omega)}$$

Impedance is generally a complex quantity:

$$Z(\omega) = Z'(\omega) + jZ''(\omega)$$

where:

- $Z'(\omega)$ is the **real part** (resistive component),
- $Z''(\omega)$ is the **imaginary part** (reactive component, associated with energy storage).

The real and imaginary components vary with frequency, therefore revealing information about different physical processes in the system.

3.3. Impedance of Ideal Elements

Understanding the impedance of ideal components is essential before addressing electrochemical systems, which are always more complex.

• Resistor (R):

$$Z_R = R$$

Purely real, independent of frequency.

• Capacitor (C):

$$Z_C = \frac{1}{i\omega C}$$

Purely imaginary and negative, indicating current leads voltage by 90°.

• Inductor (L):

$$Z_L = j\omega L$$

Purely imaginary and positive, indicating voltage leads current by 90°.

In electrochemistry capacitive behavior is often associated with **double-layer capacitance** at the electrode/electrolyte interface, while inductive features may appear due to measurement artefacts or adsorption processes.

3.4. Impedance of Electrochemical Systems

Electrochemical systems are rarely composed of pure R, C, or L elements. However, they exhibit combinations of resistive and capacitive behaviour (and occasionally inductive) due to:

- Ionic conduction in the electrolyte (resistive).
- Charge separation at the electrode/electrolyte interface (capacitive).
- Faradaic charge-transfer reactions (resistive + capacitive in parallel).
- Diffusion of ions through solid or liquid phases (frequency-dependent resistive behaviour, modelled by Warburg elements).

These phenomena have characteristic time constants and thus dominate the impedance spectrum in different frequency ranges. EIS allows us to isolate these contributions by sweeping the frequency across several orders of magnitude.

3.5. Nyquist and Bode Representations

EIS data are usually displayed in two main forms:

1. Nyquist Plot:

- Real part Z' on the x-axis, negative imaginary part -Z'' on the y-axis.
- Frequency is implicit (not shown directly on the axes).
- Each feature (semicircles, straight lines) corresponds to a specific process.

2. Bode Plot:

- Magnitude |Z| and phase ϕ versus frequency on logarithmic axes.
- Makes it easier to directly identify frequency ranges where different processes dominate.

Both forms are complementary: Nyquist plots give a geometric view of the impedance spectrum and Bode plots provide a direct frequency-process relationship.

3.6. Battery State during Measurement

Once the specific battery samples to be used in our study were selected, the next crucial step was to determine the State of Charge levels at which electrochemical impedance measurements would be performed. This choice was not arbitrary. The SoC can influence the impedance response of a battery across different frequencies, which lead to altering the magnitude and the shape of the spectrum. It is essential to understand this influence in order to evaluate whether it is possible to identify a correction factor that accounts for SoC variation. By doing so, it allows impedance-based State of Health estimations to be made at arbitrary charge levels.

In principle, such a correction could be developed if the relationship between SoC and impedance were sufficiently consistent, repeatable, and independent of other variables. However, in practice, this is almost never the case. The electrochemical processes within a lithium-ion battery can vary in complex ways as a function of SoC. When high SoC levels, for example, the electrode materials are closer to full lithiation, which typically reduces the charge-transfer resistance. When at lower SoC levels diffusion limitations and changes in the double-layer capacitance can dominate the impedance response. Some factors such as temperature and recent current history can even complicate this relationship. For these reasons, it is only possible to identify a universally applicable correction function for SoC influence under very specific and controlled conditions. Such conditions are not however representative of most real-world applications.

Therefore, the more realistic and practical approach for our study is to identify a specific SoC window in which impedance measurements give the most reliable, repeatable, and interpretable results for the specific battery model under consideration. The rest of the study can then be based exclusively on this SoC window. This design choice has an important implication for the final product that we aim to develop: the measurement system will be designed and calibrated for a specific battery type. It will also only function within the SoC range for which the system has been optimized, and its expected impedance response is well-characterized. Since the underlying electrochemical conditions would deviate from those assumed during calibration, an attempt to use the system outside this SoC range would compromise measurement accuracy.

The next step in our study was then to determine which SoC values should be included in our experimental plan. This involved a trade-off between the amount of data to be collected (and therefore the accuracy and robustness of the analysis) and the constraints of time, equipment availability, and the number of battery samples. As a result, we decided to focus on four SoC points: 100%, 80%, 50%, and 20%. This choice was guided by several considerations:

- The SoC points are placed far apart in order to capture any non-linear trends that may verify the impedance response.
- Extremely low SoC values (e.g., below 10%) were excluded, as these are rarely reached in electric vehicle operation due to range management strategies and because deep discharges can accelerate degradation.
- The selected SoC points cover the typical operational range of many lithium-ion battery applications, which make the results more relevant for cases of practical use.
- The inclusion of the 100% SoC point allows us to evaluate the impedance response under fully charged conditions. This is useful for detecting high-voltage-specific degradation effects.

Theoretical Background for Electrochemical Impedance Spectroscopy

For each of these SoC points, measurements must be performed at different SoH levels to evaluate the consistency and robustness of the impedance to SoH relationship. This requires testing cells at various stages of their life cycle, from new (SoH \approx 100%) to significantly aged. We can separate the influence of capacity fade and resistance growth from that of SoC variation, by comparing the impedance spectra at the same SoC but different SoH values. This is a crucial step in determining whether the chosen SoC point will indeed provide stable and interpretable SoH estimates.

We will use the **Coulomb Counting** method to determine the reference SoH for each battery under test.

We can track the SoH decline of each cell by performing full capacity tests throughout the aging process. Then, we can use it as the reference value against which impedance-based estimates will be compared.

The combination of these experimental parameters, which include four distinct SoC levels, multiple SoH stages, and accurate SoH reference values, will therefore generate a dataset that allows us to:

- 1. Quantify the SoC dependence of the impedance spectrum for the selected battery model.
- 2. Identify the SoC point at which SoH estimation via EIS is least affected by the SoC-induced variability.
- 3. Provide a calibrated basis that serves for the design of a measurement device that operates reliably within a specified SoC window.

4. Artificial Aging of Lithium-Ion Batteries

The cell selected for this dissertation is a cylindrical 18650 cell. This cell is chosen for its wide availability and its LiMn₂O₄-based chemistry, which exhibits electrochemical behavior comparable to that of batteries commonly employed in automotive applications.

A set of selected batteries was subjected to a controlled artificial aging process to obtain cells at different degradation levels required for impedance measurements. The aim of this selection was to create multiple samples for each target State of Health level, approximately 100%, 90%, 80%, and 70% with more than one sample per level to improve statistical robustness. This made sure that any relationship that was observed between impedance and SoH could have been validated through repeated measurements and was not influenced by single-cell anomalies. The result was a comprehensive SoC–SoH measurement matrix with reliable and repeatable data that covered a wide range of degradation states.

4.1. Battery Aging Mechanisms

Lithium-ion battery aging is the result of multiple chemical, electrochemical, and mechanical phenomena that occur during both use and storage. These processes cause a gradual loss of capacity over time, including an increase in internal resistance, and a reduction in overall efficiency. The most relevant mechanisms for this study are:

- Solid Electrolyte Interphase (SEI) growth
- Loss of Lithium Inventory (LLI)
- Loss of Active Material (LAM)
- Electrolyte decomposition
- Structural degradation of electrodes
- Current collector corrosion

It will be explored more in deeply about this phenomenon in next chapters.

4.2. Factors Accelerating Battery Aging

Battery aging can be influenced by several external and operational factors. Controlling these following factors is key when designing an artificial aging protocol:

- **Temperature**: High temperatures (>40 °C) accelerate reaction kinetics, which promote faster SEI growth and electrolyte decomposition. However, excessive heat (>60 °C) can trigger dangerous conditions.
- **State of Charge**: Prolonged high SoC storage increases the oxidative stress on the cathode and promotes metal dissolution and electrolyte oxidation. Very low SoC can destabilize the SEI and eventaully cause copper dissolution.

- **Depth of Discharge (DoD)**: Deep cycling increases mechanical strain on electrodes due to expansion and contraction, which leads to particle cracking and delamination.
- **C-rate**: High charging or discharging rates cause significant ohmic heating, exacerbate lithium plating risk, and create non-uniform current density across the electrode surface.
- **Voltage extremes**: Operation close to the maximum or minimum voltage limits will accelerate unwanted side reactions at both electrodes.

These factors dictate the rate at which a cell degrades in real applications, while also providing levers for accelerating aging in laboratory conditions without deviating too far from realistic mechanisms.

4.3. Artificial Aging Protocol

The artificial aging process was designed to replicate the most influential real-world degradation mechanisms in a compressed timescale. It combined partial SoC cycling with elevated temperature storage to induce SEI growth, active material loss, and lithium inventory depletion in a controlled manner.

4.3.1. Initial Characterization

Before aging each cell underwent:

- Full charge to 100% SoC according to manufacturer's specifications.
- Capacity test at 0.5C to establish baseline capacity.
- Calculation of initial SoH via Coulomb counting:

$$SoH = \frac{C_{measured}}{C_{rated}} \times 100\%$$

• Initial EIS measurements at all SoC points selected for the study (100%, 80%, 50%, 20%).

These baseline measurements made sure that subsequent changes could be directly attributed to the aging process.

4.3.2. Cycling Conditions

Cells were cycled between 10% and 90% SoC to apply both lithiation and delithiation stresses without exposing them to extreme voltages.

• Charge profile: Constant current—constant voltage at 1C until the upper SoC limit was reached.

- **Discharge profile**: Constant current at 1C down to the lower SoC limit.
- **Rest periods**: Minimal, in order to maximize the number of cycles completed within the available time.

This cycling window was chosen to reflect the typical operational patterns in electric vehicles, while avoiding very low SoC regions that could then accelerate harmful copper dissolution.

4.3.3. Temperature Control

Cells were placed in a climatic chamber maintained between 40 °C and 45 °C. This temperature range accelerates chemical reactions such as SEI growth and electrolyte breakdown without causing thermal damage. Controlled heating also ensures consistency across all samples.

4.3.4. Periodic Assessment

Every 50 cycles, aging was paused to perform:

- Capacity test at 0.5C to update the SoH.
- EIS measurements at each SoC point to monitor impedance of evolution.

This periodic assessment allowed for real-time tracking of degradation and timely removal of cells from the protocol upon reaching their target SoH.

4.3.5. Achieving Target SoH Levels

By applying identical conditions but stopping cells at different points in their degradation curve:

- SoH 100% group: unused cells stored under optimal conditions.
- SoH 90% group: cells removed after ~200–250 cycles.
- SoH 80% group: cells aged further until ~350 cycles.
- SoH 70% group: longest-aged group often exceeding 500 cycles.

At least two cells were prepared for each SoH level to allow averaging and identification of outliers.

4.3.6. Safety and Monitoring

Throughout the process:

• Voltage, current, and temperature were continuously monitored.

Artificial Aging of Lithium-Ion Batteries

- Internal resistance was checked via pulse testing.
- Cells were visually inspected for swelling, leakage, or discoloration.

Any cell showing any abnormal behaviors was removed in order to maintain the integrity of the dataset.

4.3.7. Relevance to the Study

The artificial aging process produced a set of cells that represented realistic degradation states within a reduced timeframe. The methodology ensured that the resulting samples captured the multi-faceted nature of lithium-ion battery aging, by targeting both capacity fade and impedance growth. This approach provided:

- A controlled and repeatable way to populate the SoC–SoH test matrix.
- Multiple physical samples per SoH level to increase confidence in statistical analysis.
- Degradation mechanisms that similarly match those found during practical applications.

The dataset obtained from these artificially aged cells would form the foundation for analyzing the relationship between EIS parameters and the SoH which ultimately guides the selection of an optimal SoC range for reliable health estimation.

5. Experimental Setup and Methodology

The experimental activity was dedicated to performing Electrochemical Impedance Spectroscopy on cylindrical 18650 lithium-ion cells. The primary objective was to obtain reproducible and high-fidelity impedance spectra across a wide frequency range. In order to achieve this, it was necessary to have a careful design of the measurement chain, a controlled environment, and systematic validation of every instrumental component involved.

5.1. Measurement Architecture

The experimental setup was centered around a modular electrochemical workstation operating as potentiostat and galvanostat with an integrated Frequency Response Analyzer (FRA). This device provided stable operation over frequencies spanning from the sub-Hz to the MHz range, which allowed us to capture kinetic and diffusion-related processes.

The workstation incorporated signal generation, data acquisition, and control logic into a single unit. This helped to reduce synchronization errors that are common in multi-instrument configurations. Despite its versatility, specific attention had to be paid to the **low-frequency regime.** Here, long acquisition times expose the measurements to drift and external disturbances.

5.2. Auxiliary Equipment and Conditioning

Each measurement required the cell to be brought to a precise SoC. A programmable DC power supply was used for controlled charging via a standard **constant-current/constant-voltage (CC-CV)** protocol, while a programmable electronic load handled the discharging. These instruments offer a fine current and voltage resolution which allows reproducibility between tests and preventing overcharge or thermal stress.

Each conditioning phase was followed by a rest period until both voltage and temperature reached equilibrium in order to make sure that the impedance spectra reflected electrochemical behavior rather than transient effects. Even though initially underestimated, this equilibration step proved to be an essential way to avoid any artificial shifts in the mid-frequency region of the Nyquist plot.

5.3. Temperature Control and Monitoring

Because impedance is very temperature-dependent, **thermal stability** was treated as a critical parameter rather than a background condition. Each cell was equipped with a type-K thermocouple fixed near the negative terminal with Kapton tape. This guaranteed electrical insulation and good thermal contact. Temperature was logged with 0.1 °C resolution throughout all measurements.

Early trials showed that even minor fluctuations (~1 °C) could produce detectable changes in the charge-transfer resistance. As a consequence, the entire setup was operated in a thermally regulated laboratory, and all equipment was powered well in advance to allow internal stabilization.

5.4. Electrical Connections and Mechanical Stability

Although it may appear trivial, the connection interface between the analyzer and the cell became one of the dominant sources of measurement uncertainty. Standard alligator clips introduced variability in the high-frequency region because of unstable contact resistance. This was eliminated by adopting **Kelvin connections**, where separate paths are used for current injection and voltage sensing.

5.5. Calibration and Verification Procedures

Instrumental reliability was verified periodically through **open/short/load** calibration routines. This compensated for cable parasitic and ensured accurate impedance readings over the entire frequency spectrum. Complementary tests on known RC reference networks provided additional validation for magnitude and phase accuracy.

Repeatability tests were performed on a dedicated reference cell kept at constant SoC and temperature. All of these tests served to quantify the inherent variability of the system and detect any drift caused by contact degradation or environmental changes. Through these measures, reproducibility was better than ± 1 % in ohmic resistance and ± 3 % in charge-transfer resistance was routinely achieved.

5.6. Mitigation of Measurement Artifacts

Two classes of disturbances emerged as critical during the campaign.

At **low frequencies** (<0.05 Hz), the long sampling intervals rendered the measurement sensitive to external vibrations and slow drifts. This was mitigated by scheduling these scans during low-activity periods and isolating the test bench mechanically.

At **high frequencies** (>100 kHz) electromagnetic interference from laboratory electronics became prominent. Grounded shielding panels, ferrite chokes, and optimized cable routing were introduced, which led to a substantial reduction in spectral noise.

5.7. Data Handling and Traceability

Each measurement was automatically logged into CSV format. It was accompanied by metadata including cell ID, SoC, temperature, and instrument configuration. Data integrity was maintained through a dual-backup strategy involving local and network storage. A structured database indexed all experiments, which eventually facilitated a later retrieval and cross-comparison.

5.8. Overview

The combination of accurate instrumentation, robust thermal control, and meticulous calibration routines allowed the experimental campaign to generate a consistent and reproducible dataset. Each refinement in the setup, from the adoption of Kelvin clips to the enforcement of equilibration times, contributed to the reduction of systematic uncertainty and to the reliability of the impedance measurements.

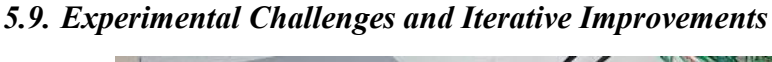




Figure 5: first measurement attempt layout

The experimental activity was marked by a continuous process of refinement despite the robustness of the setup. The first measurement sessions revealed a series of subtle but recurring issues that required procedural adjustments and small practical improvements to the test environment.

One of the most persistent difficulties was the **stability of the low-frequency points**. Because each impedance value at 0.01 Hz required several minutes of acquisition. Even minor disturbances, such as vibrations from nearby instruments or mechanical shifts of the table, could distort the phase response. Measurements in the low-frequency region were performed during quiet periods to mitigate these effects. The workbench was **mechanically isolated** using simple rubber dampers placed under its legs. This small but significant modification was proved to be effective in reducing vibrations transmitted through the floor and improved the repeatability of the low-frequency measurements.

At the same time, **electromagnetic interference** was identified as a limiting factor at high frequencies. Early spectra displayed characteristic ripples attributable to surrounding electronic equipment. A straightforward mitigation strategy was adopted. All **non-essential devices in**

the laboratory were switched off during EIS acquisition, and the measurement cables were kept as short as possible and routed away from power lines. Moreover, ferrite beads were added to the most sensitive signal cables, which provided a noticeable reduction of high-frequency noise above 50 kHz.

These simple yet effective measures, alongside greater attention to environmental conditions, led to a significant improvement in the **signal quality and overall reproducibility** of the measurements, which did not require any complex or costly modifications to the setup of the laboratory.

5.10. Optimization of the Contact Interface

Mechanical contact variability proved to be a very important data quality determinant. Even small differences in pressure or positioning of the clips produced measurable shifts in the ohmic resistance. The transition from generic alligator clips to rigid **Kelvin-type holders** marked a turning point in the campaign.

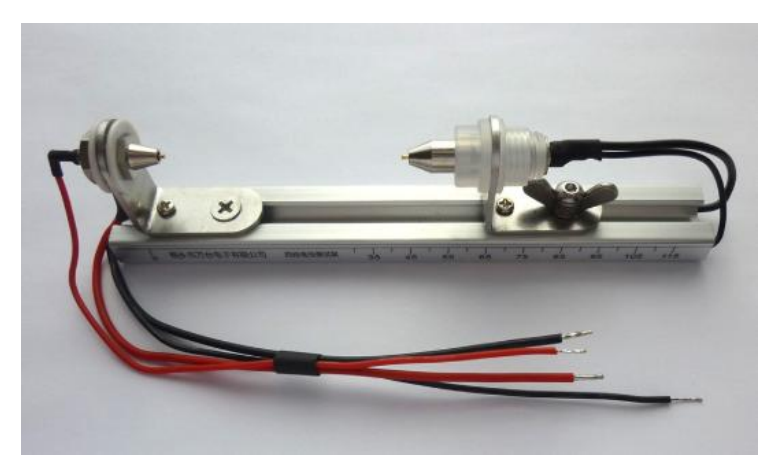


Figure 6: battery holder

Each holder was designed to maintain a fixed geometry and a repeatable alignment with the cell terminals. The 3D printed fixtures were also used as a partial vibration damper, which further stabilized the setup. As a result, the high-frequency intercept of the impedance spectrum, which was a sensitive indicator of contact resistance, became highly consistent across repetitions.

Figure 5.1:

5.11. Control of Electrochemical Conditioning

Some early attempts at rapid cycling between different states of charge revealed the importance of **electrochemical relaxation**. Measurements that were performed immediately after charging or discharging displayed transient voltage drift and temperature gradients that

could not be distinguished from real impedance changes. Successive protocols introduced mandatory rest phases, which were empirically optimized for each SoC level. These pauses, which typically lasted between 20 and 45 minutes, allowed the cell to return to near equilibrium before the EIS scan.

Furthermore, the current rates for charge and discharge were limited to moderate values (C/2 or 1C) in order to prevent local heating and to also minimize electrolyte polarization. This conservative approach helped only slightly to extend the overall duration of the campaign but ensured that impedance variations reflected a genuine electrochemical behavior rather than thermal artifacts.

5.12. Calibration Frequency and Reference Validation

Even high-quality measurement instruments exhibit **drift** over time. Probably, this was due to connector wear, temperature cycling, or software updates, or even a combination of some of them. Calibration routines were performed to maintain reliability at the start of each measurement week and whenever anomalies were detected.

5.13. Repeatability Assessment

The credibility of the EIS dataset was anchored in repeatability testing. A single **reference cell** stored at 50% SoC served as a long-term benchmark throughout the campaign. Its impedance spectrum was measured weekly to monitor any instrumental drift. The variations in the high-frequency resistance stayed within $\pm 1\%$, while the mid-frequency semicircle diameter fluctuated within $\pm 3\%$. These figures were consistent with the intrinsic precision limits of the instrumentation and confirmed the overall stability of the experimental procedure.

5.14. Consolidation of Best Practices

As the campaign progressed, the iterative refinement of methods converged into a set of operational "best practices" that improved data quality and efficiency in a substantial way. Among the most impactful there were:

- Thermal equilibration that before every scan allowed for a stable impedance baseline.
- **Fixed mechanical geometry** for all connections which led to eliminating contact variability.
- **Regular calibration and reference validation** used as a part of the standard workflow.
- Systematic data organization which enabled traceability and error tracking.
- Noise mitigation and bench isolation, which extended the usable frequency range.

Together, these measures transformed, what initially appeared as a straightforward measurement task, into a rigorously controlled experimental process. The dataset that resulted was consistent across all repetitions, resilient to environmental disturbances, and was suitable for advanced electrochemical interpretation in the subsequent analyses.

5.15. Preliminary Data Validation and Quality Assessment

A systematic verification phase was introduced, upon completion of the first consistent series of measurements, as a way to make sure that the collected impedance data were technically reliable and physically meaningful. Since the Electrochemical Impedance Spectroscopy was seen to have sensitivity to even minor disturbances, the raw data could not be considered trustworthy without putting in place a structured post-acquisition screening process.

The goal at this stage was not yet to extract electrochemical parameters, but it was to only **confirm the internal consistency and plausibility** of the acquired spectra before including them in the central dataset.

A lightweight **Matlab-based script** was developed to automatically read the CSV files exported by the impedance analyzer and to generate quick visualizations of the Nyquist and Bode plots. An intentionally simple code allowed to identify obvious anomalies directly after each measurement. Such anomalies include non-physical negative imaginary components, discontinuities between frequency decades, or abrupt noise bursts.

Each dataset was plotted in its raw form, without any filtering or curve fitting, in order to avoid the masking of possible acquisition errors. The overlays between repeated scans of the same cell provided an immediate visual confirmation of repeatability of the measurement. The corresponding test was marked for repetition and excluded from the main archive until verification, when deviations larger than the established thresholds were observed.

5.16. Data Screening Criteria

The validation process was guided by a few essential criteria, which were developed empirically over the first weeks of testing.

- **Spectral continuity:** the impedance curve had to evolve smoothly with frequency, without jumps or isolated points inconsistent with neighboring values.
- **High-frequency intercept consistency:** repeated measurements under identical conditions were required to show less than $\pm 1\%$ deviation in ohmic resistance.
- Low-frequency convergence: the real component of impedance had to stabilize within a finite range. Unbounded growth or oscillations indicated drift or noise contamination.
- **Temperature coherence:** the recorded temperature trace during each scan was cross-checked. Any fluctuation above 0.5 °C during the frequency sweep led to rejection of the data.

Such a structured filtering step was proved to be an invaluable tool in maintaining dataset integrity. Especially when accumulating large volumes of measurements over extended time periods. In practice, roughly 8-10% of the initially collected spectra were discarded during this quality control phase, most of the time due to thermal instability or minor contact perturbations that were identified in the visual plots.

5.17. Observations and Incremental Refinements

Several subtle patterns became apparent through repeated use of this validation tool. For instance, the measurements that were conducted immediately after the cell mounting displayed small but systematic offsets in the high-frequency region. This was attributed to incomplete mechanical stabilization. Extending the rest before the start of the scan by just a few minutes eliminated this shift effectively.

In a similar way, the Nyquist visualizations sometimes revealed slight asymmetries between forward and backward frequency sweeps. This is a sign of residual drift in the potentiostat's DC bias. The recalibration and a prolonged warm-up period were proved to be sufficient to restore symmetry and improve reproducibility.

The iterative nature of this process, which includes alternating between measurement, quick visual validation, and procedural adjustment, was able to progressively refine the experimental setup and operator confidence. While it was very simple in concept, this early-stage quality control established a **feedback loop** that helped preventing the accumulation of corrupted or inconsistent data. This eventually saved a significant effort during later analysis phases.

5.18. Summary of Experimental Reliability

By the conclusion of this phase, the workflow had evolved into a robust pipeline capable of generating high-quality and self-consistent impedance data. Each measurement was automatically accompanied by its diagnostic visualization and metadata record. This allowed the dataset to grow in a **structured and traceable** manner.

The combination of rigorous measurement conditions, systematic calibration, and immediate post-acquisition validation made sure that only spectra meeting defined stability and coherence criteria were retained for subsequent analysis.

5.19. Residual Limitations and Practical Considerations

Despite the high level of control achieved, some inherent limitations remained. The **low-frequency domain** continued to pose practical challenges. Even under optimized conditions, measurements below 0.02 Hz required a prolonged acquisition time, during which small thermal or voltage drifts could still influence the phase response. In a similar way, the **upper-frequency limit** was constrained by the analyzer's internal bandwidth and the parasitic inductance of the connection leads.

Another persistent factor was **temperature uniformity within the cell**. Although the external temperature was precisely monitored, minor gradients between the surface and core could not be entirely ruled out. This happened especially after extended charge or discharge conditioning. These effects were minimized but not eliminated. They also represent one of the

unavoidable uncertainties in EIS performed on sealed commercial cells without embedded sensors.

5.20. Data Robustness and Reproducibility

Within these boundaries the overall **data robustness** was deemed satisfactory for subsequent interpretation. The measured impedance spectra displayed consistent topology across repetitions: stable high-frequency intercepts, well-defined mid-frequency arcs, and coherent low-frequency tails. These repetitions indicate that the measurement system effectively captured the electrochemical response of the cells rather than artefacts of the setup.

Repeatability tests on multiple days confirmed that the variability between independent measurements remained within a narrow and quantifiable margin, once the experimental environment and connection geometry were stabilized. The dataset that resulted from that satisfied the core criterion of **internal reproducibility**, which is a prerequisite for any subsequent analysis of degradation trends or equivalent-circuit modeling.

5.21. Lessons from the Experimental Campaign

From a methodological perspective, the experimental phase highlighted several broader lessons that extend beyond the specific case of EIS on lithium-ion cells. Chief among them is the realization that **measurement precision is not purely a function of instrument performance**, but equally of mechanical and procedural consistency. The most impactful improvements often came from attention to detail in contact quality, equilibration times, and calibration discipline, not from new hardware.

The same importance was the integration of **real-time quality control** through the quick plotting script and a structured data management system. This practice transformed data validation from a retrospective correction step into an integral part of the measurement routine, which prevented error propagation.

Finally, the gradual codification of operational rules, such as minimum stabilization times, acceptable temperature deviations, and criteria for data acceptance, turned what was, initially, an empirical process into a **replicable experimental framework**. The result was not a collection of impedance measurements, while also it validated procedure capable of producing meaningful data under controlled and repeatable conditions.

6. Physical principles of degradation in lithium-ion batteries

6.1. Overview: what really "ages"

When we say that a battery "ages", two macroscopic two quantities change: the **capacity** (how much change can still hold) and **deliverable power** (how rapidly can exchange that charge without overheating or drop too much in voltage. At microscopic level, these two effects stem from three categories of causes that often coexist:

- Loss of Lithium Inventory (LLI): Part of the cyclable lithium is "trapped" in reaction products (for example, in SEI or as plated lithium metal). Capacity decreases because there is less lithium available for intercalation/deintercalation.
- Loss of Active Material (LAM): A portion of the electrode material (anode or cathode) becomes electrically or ionically isolated (cracking, detachment from the collector, percolation loss), or chemically inactive (phase transitions, surface degradation). Capacity and power decrease together.
- Increase in Internal Resistance: The barrier to the passage of ions and electrons increases (thicker/more disordered interface layers, reduced porosity, slower diffusion, poorer contacts). Power decreases and greater ohmic losses are observed.

Degradation can be **scheduled** (even at still battery it depends mostly on temperature and storage charge status) or **cycled** (induced by the passage of charge, therefore by currents, discharge depth, charging speed, etc.). The underlying physical mechanisms are the same but activated with different intensity depending on operating conditions.

6.2. Interfaces and layers: SEI and CEI

6.2.1. SEI on the anode (Graphite/Silicon)

At the anode (typically graphite, sometimes with a fraction of silicon), the organic electrolyte **reduces** during the first charges, forming the **Solid Electrolyte Interphase**: a nanometric layer that is ionically conductive but electrically insulating. It is essential (passive electrode), but continues to **grow** slowly over time, consuming lithium:

- Diffusion-limited growth: usually it is observed $x_{SEI}(t) \propto \sqrt{t} \rightarrow \text{lost capacity}$ for LLI $\propto \sqrt{t}$
- Consequences: increased charge transfer resistance, power drop, and cumulative loss of cyclable lithium.

Silicon amplifies the problem: volumetric expansion of up to ~300% during Li–Si alloying causes recurrent cracking, exposing virgin surface. SEI breaks down and reforms cycle after cycle, accelerating LLI and LAM.

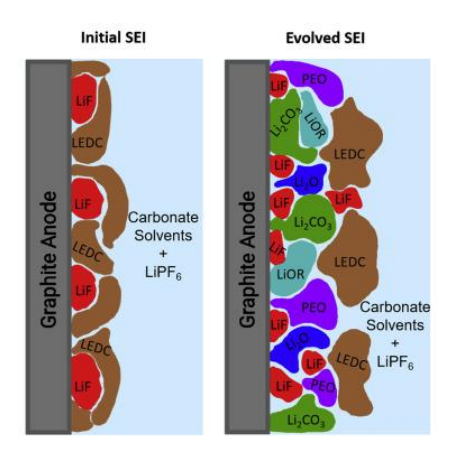


Figure 7: SEI formation

6.2.2. CEI on the cathode

At high potentials, the cathode oxidizes the electrolyte, forming a **Cathode-Electrolyte Interphase** (CEI). This layer can **stabilize** the surface but, if disordered or too thick, increases surface resistance. On high-nickel materials (NMC/NCA high-Ni), electrolyte oxidation and the release of lattice oxygen at high voltages accelerate the growth of "hard" and reactive CEI.

6.3. Lithium plating

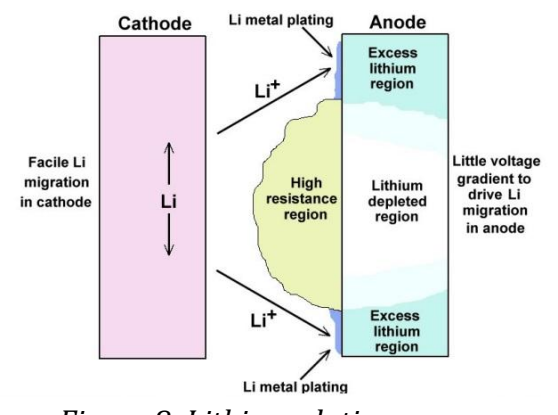


Figure 8: Lithium plating process

When the local potential of graphite drops too close to 0 V vs Li/Li⁺ (for low temperatures, high charging currents, nearly saturated anodes, or polarizations due to high resistances), it becomes thermodynamically advantageous to deposit lithium metal rather than intercalate it:

- **Nucleation and growth**: initially "islands" of metallic Li; under severe conditions, filaments/dendrites that can cross the separator.
- Irreversible vs. reversible: a fraction can "reinsert itself" during the next discharge; the rest is isolated and then consumed by secondary reactions. → LLI.

• Consequences: decrease in capacity (LLI), increase in surface resistance, risk of internal short circuit and gas formation (due to reactions between lithium metal and electrolyte).

The safe **operating window** for fast charging is therefore limited by the temperature, the current, and the anode filling status.

6.4. Cathode degradation: chemistry, structures, and transition metals

6.4.1. Dissolution of transition metals

In materials such as LMO (spinel), there is disproportionation.

$$2Mn^{3+} \rightarrow Mn^{2+} + Mn^{4+}$$

where Mn²⁺ dissolves in the electrolyte, migrates and deposits on the anode, catalyzing further SEI growth and parasitic reactions. Even in NMC/NCA there can be dissolution (Ni/Co/Mn) especially in high voltage or in the presence of HF. The result: LAM to the cathode and accelerated aging of the anode.

6.4.2. Oxygen release and phase transitions

Ni-rich cathodes are more energetic but more delicate: high stresses and high temperatures can release reticular oxygen, triggering electrolyte oxidation (unstable CEI), heating, and microcracking of particles (LAM). Locally, the surface can be transformed into unproductive **rock-salt-like phases**, which electrically isolate some portions of active material.

6.4.3. Cracking from "lattice breathing"

During (de)intercalation, the cathode lattice parameter "breathes." Repeated over time, this induces mechanical stress and intergranular microfractures; fragments may lose contact with the binder/collector. \rightarrow LAM and increase resistance.

Note: cathodes such as LFP exhibit excellent thermal/structural stability. They degrade more slowly but are not immune to percolation loss or resistive IEC at high voltages.

6.5. Electrolyte and conductive salt: basic chemistry

The most common salt, **LiPF**6, it is convenient but **unstable**: in the presence of traces of water, the following reaction occurs:

$$LiPF_6 + H_2O \rightarrow LiF + POF_3 + 2HF.$$

HF attacks the cathode surfaces (promoting the dissolution of transition metals) and reacts with SEI species, making it more fragile and consuming additional lithium. Solvents such as EC/EMC can oxidize at high potential (cathode) or reduce (anode), generating solid species.

(Li₂CO₃, LiF, LEDC) and **gas** (CO₂, CO, H₂), with cell **swelling** and increased ionic **resistance** in the pores.

Additives (e.g., VC, FEC) help to form more stable SEI/CEI, but at high temperatures even additives are depleted, and the benefits diminish.

6.6. Mechanics and percolation: when the structure breaks down

The heart of LAM is often mechanical:

- **Graphite anode**: deep cycles and/or rapid charging generate Li and strain gradients; particulate matter can crack, losing contact with the binder.
- **Silicon**: enormous cyclic expansion/contraction causes pulverization; without containment strategies (nanostructuring, elastic binders, pre-lithiation), percolation loss is rapid.
- Cathode: microcracks open new reactive surfaces → more CEI, more indirect LLI, and electronic isolation of fragments.

The **effective porosity** of the electrode tends to decrease due to pore collapse and filling with solid products \rightarrow **tortuosity** increases \rightarrow slower ion diffusion \rightarrow more polarization and heat.

6.7. Extreme events: over-discharge, over-charge, and safety

- Over-discharge can push the anode towards potentials that lead to the dissolution of the copper in the collector. Cu⁺ can then redeposit as metal filaments, creating permanent micro-cuts.
- Over-charging (beyond the voltage limit) accelerates electrolyte oxidation, oxygen release from the cathode, and triggers exothermic reactions.

The simplified **heat balance** includes ohmic heat. I^2R and the **entropic** heat $I^T \frac{\partial E_{\text{OCV}}}{\partial T}$. If generation exceeds dissipation, the temperature rises. Parasitic reactions accelerate (Arrhenius), and in extreme cases, a runaway occurs. The separator (PE/PP) can shrink beyond ~120–140°C, increasing the risk of a short circuit.

6.8. Map of operating conditions

Temperature

• **High T**: accelerates all parasitic reactions (SEI/CEI growth, dissolution, gas).

• Low T: worsens kinetics/diffusion → more plating during charging and mechanical stress.

SoC and window of use

- **High SoC at rest** promotes cathode oxidation and metal dissolution (calendar).
- Extreme low SoC: increases the risk of copper dissolution in overcharging.
- Narrow window (e.g., 20–80%) reduces stress peaks and prolongs life.

Current/C-rate and charging profiles

- **High C**: large $|\eta|$ large concentration gradients and heating \rightarrow accelerate LLI/LAM.
- **Fast charging**: requires thermal management and adaptive limitations (current reduction at unfavorable SoC/T) to prevent plating.

6.9. Internal heterogeneity and "uneven aging"

In the actual cell, there are **local gradients** in temperature, Li concentration, and current. Coating imperfections, uneven distribution of particles/binder, or slight differences in contact pressure lead to hot spots and starved areas. These regions degrade first (more SEI, more cracking, more CEI), starting a vicious cycle: more resistance \rightarrow more heat/local polarization \rightarrow even more degradation.

At the pack/module level, small differences between cells lead to imbalance: some cells operate at higher SoC or at different temperatures, aging faster and dragging down the system.

6.10. Macroscopic observations and "signatures" of mechanisms

Without introducing circuit models yet, the above mechanisms have diagnostic traces:

- Capacity and Coulombic Efficiency: CE < 100% on average indicates systematic consumption of LLI.
- **Increased resistance** (DCIR, power fade): indicates growth of interface layers, loss of percolation, or worsened transport in the pores.
- Incremental Capacity (dQ/dV) / Differential Voltage: the shift/attenuation of peaks related to intercalation stages (graphite) or cathode transitions suggests LLI vs. LAM and structural changes.
- **Self-discharge and gas/swelling**: indicate high electrolyte reactivity, unstable CEI/SEI or soft shorts.
- Increasing **OCV hysteresis** indicates greater internal resistance and inhomogeneity.

6.11. Engineering and control implications

• **Thermal management**: keeping the cell within an optimal thermal window limits both plating (cold) and parasitic reactions (hot).

- Usage policy: avoid long storage at very high SoC, limit extreme daily DoD, prefer well-calibrated step-down or CC-CV charging profiles.
- **Materials and design**: cathode surface coatings, electrolyte additives, elastic binders for Si, porous architectures with low tortuosity, and robust conductive collectors/lattices mitigate LAM/LLI.
- Pack-level equalization and balancing mitigate heterogeneity and dilute stress peaks on individual cells.

6.12. Operative summary

- LLI is driven by SEI/CEI, plating, and parasitic reactions; it increases with T, high SoC at rest, and fast charging under unfavorable conditions.
- LAM arises from cracking, loss of contact, and structural transformations; it worsens with high currents, Li gradients, and mechanically fragile materials (Si, high-Ni without mitigation).
- The increase in resistance is the cross-sectional result of thicker interface layers, clogged pores, and weakened electronic percolation.

These mechanisms build the conceptual bridge between physical-chemical phenomenology and the quantities that we then measure in diagnostics: capacitance, resistance, voltmetric signatures, and response spectra. In the following chapter, we will use this cause—effect map to justify modeling choices and parametric identification tools.

6.13. Transition towards model representation

At this point, a common thread can be identified: every physical degradation phenomenon, despite having distinct chemical, structural, or mechanical origins, always results in a change in the cell's electrical response. This observation is the reason why diagnostic methods, such as Electrochemical Impedance Spectroscopy, are so effective: since each transport or reaction process is associated with a characteristic time constant, its evolution over time (and therefore degradation) manifests itself as a variation in the distribution of these time constants, and therefore in the overall shape of the impedance spectrum.

Before moving on to electrical modeling, it is useful to explain how the phenomena discussed in the previous paragraphs influence the parameters that will subsequently be represented by circuit elements.

6.13.1. Influence of SEI and LLI on electrical response

SEI growth, as we have seen, it is a phenomenon that often follows a law such as \sqrt{t} . At the electrical level, this corresponds to a progressive increase of the charge transfer resistance and a decrease in apparent double layer capacity, as part of the electroactive surface is shielded.

SEI also acts as a **diffusion barrier**: Li⁺ ions must cross a layer of increasing thickness and complex structure. This introduces a phase delay in responses at intermediate and low frequencies, which appears in a Nyquist diagram as a wider semicircle or a non-ideal slope (no longer perfectly capacitive).

From the point of view of macroscopic parameters, this translates into an increase in polarization resistance and a slowdown in dynamic response.

6.13.2. Plating and nonlinear polarizations

Lithium plating has mixed effects:

- Initially, metal deposition increases surface conductivity, but not uniformly; as the phenomenon evolves, inactive and insulating areas of form, increasing resistance.
- The interaction of metallic lithium with electrolyte generates new compounds. (Li2CO 3, LiF, ecc.), which amplifies the growth of SEI and therefore the low-frequency resistive part of the spectrum.
- At the macroscopic level, plating alters Coulombic reversibility: part of the charge introduced is no longer recoverable, highlighting a structural and permanent LLI.

These effects are reflected in a **non-linear** response to high currents and a progressive shift of the low-frequency regions of the Nyquist diagram, where diffusion and slow reactions dominate.

6.13.3. Cracking and loss of percolation (LAM)

When a portion of active material loses electrical contact, the effective active surface area is reduced. In electrical terms, this corresponds to a decrease in the effective capacity of the electrode and a change in the local time constants. The system becomes more heterogeneous: not all particles react in the same way and in the same frequency range, so the impedance spectrum shows a broadening of the transition regions (wider semicircles, smoother slopes). In practice, this reflects a continuous distribution of relaxation times, often modeled through non-ideal elements such as the **Constant Phase Element (CPE)**, which will be introduced in the next chapter.

6.13.4. Cathode effects and dissolution of transition metals

The dissolution of metals such as Mn, Ni, and Co modifies both the cathode and anode surfaces. On the cathode, the loss of active material and the formation of a thick IEC increase the resistance associated with charge transfer; on the anode, the deposited metals catalyze undesirable reactions that lead to accelerated SEI growth and, therefore, to further overall polarization of the system. In the frequency domain, these processes manifest themselves as an increase in series esistive and capacitive components, but with longer relaxation times, typical of the low-frequency regions of the spectrum.

6.13.5. *Ionic diffusion and slow transients*

The slowing down of internal diffusion processes (both in the electrodes and through the SEI/CEI) results in a non-instantaneous response to potential changes.

Mathematically, diffusion is described by:

$$Z_W = \sigma_W \frac{\tanh(\sqrt{j\omega\tau_W})}{\sqrt{j\omega\tau_W}},$$

Where σ_W is the Warburg coefficient and τ_W the diffusion time constant.

When diffusion is severely limited or the surface becomes uneven, the real and imaginary parts of the impedance show a **45°** trend in Nyquist, typical of semi-infinite diffusion. With aging, this trend tends to shift to the right and lengthen, indicating slower diffusion or a thicker layer to pass through.

6.13.6. Thermal effects and reversible variations

Some variations in electrical parameters may be **reversible** if induced by temperature changes. An increase in T temporarily reduces diffusion and charge transfer resistance, but in the long term accelerates structural growth. Conversely, at low temperatures, diffusion slows down and the system exhibits higher impedances at high frequencies, an effect that can be mistaken for degradation if the thermal component is not taken into account. It is therefore essential to distinguish between **temporary** (environment-dependent) and **permanent** (physical-chemical deterioration-related) variations.

6.13.7. Phenomenological synthesis

We can therefore map in qualitative form the direct links between degradation mechanisms and measurable electrical quantities:

Physical phenomenon	Macroscopic effect	Observable electrical effect
SEI / CEI growth	LLI increase, interface resistance	Rightward shift of the high-frequency semicircle
Li plating	LLI, short-circuit risk	Increased resistance at low frequencies, non-linear variations
Cracking / LAM	Loss of active capacity	Equivalent capacity reduction, wide semicircles (time distribution)
Slowed spread	Polarisation, power drop	More extensive 45° slope (Warburg)
Metal dissolution	Unstable CEI, cross-talk	Increase in overall polarisation
Temperature increase	Acceleration reactions	Faster transients but faster degradation
High current	Polarisation and stress	Expansion of intermediate impedance regions

This table establishes a conceptual link between degradation chemistry and circuit modeling: each physical process can be represented by an element, or a set of elements, capable of reproducing its dynamic effect on the overall impedance.

7. Equivalent Circuit Model for Ageing Phenomena in Lithium-Ion Batteries

7.1 Introduction

The experimental results obtained through Electrochemical Impedance Spectroscopy are valuable on their own, but their interpretability and predictive power increase significantly when they are mapped to a **mathematical-physical model** of the system. The most widely adopted approach in electrochemistry for this purpose is the construction of an **Equivalent Circuit Model (ECM).** ECM is an arrangement of idealized electrical components such as resistors, capacitors, and special impedance elements. Each of these components is associated with a specific physical or chemical process that occurs inside the cell.

An ECM is not just a curve-fitting tool. It also embodies a *hypothesis* about underlying physics. The value of each component is expected to change in a predictable way with the cell's state of charge, state of health, temperature, and usage history. The selection of components, and thus the selection of which physical phenomena to represent explicitly, is therefore an important step. In this study, the ECM was designed to focus on the **dominant ageing mechanisms** that are measurable via EIS and relevant for long-term capacity fade and power fade in lithium-ion cells.

7.2 Modeling using equivalent circuits

Experimental analysis of electrochemical impedance provides a wealth of information about the internal behavior of the battery, but experimental data alone, represented for example in the Nyquist complex plane, is not sufficient to describe the physicochemical phenomena occurring inside the battery in a quantitative and reproducible manner. This is why it is essential to use an ECM, which allows the electrochemical behavior of the system to be translated into an analytical and calculable form.

The idea behind this approach is to replace the dynamic behavior of the cell with a network of ideal electrical elements, resistors, capacitors, and, in some cases, constant phase elements (CPEs), whose frequency response accurately reproduces the experimentally measured impedance curve. In other words, the equivalent circuit becomes a tool for emulating the actual behavior of the battery.

Based on experimental data (Z_{real}, Z_{imag}, f) ,

the values of the circuit components are identified such that

$$Z_{\text{modello}}(f) \approx Z_{\text{misurato}}(f)$$

for each frequency within the analysis window.

7.3 From experimental measurement to analytical model

Each point on the Nyquist diagram corresponds to a complex impedance measurement. $Z(f) = Z_{\text{real}}(f) + jZ_{\text{imag}}(f)$, obtained by applying a small amplitude sinusoidal signal with

variable frequency to the battery. The objective of the modeling is to determine a complex function $Z_{eq}(f)$ derived from an equivalent circuit that satisfies the relationship:

$$Z_{\text{eq}}(f) = f(R_i, R_{ct}, C_{dl}, \text{CPE}, W, ...)$$

Where the parameters R_i , R_{ct} , C_{dl} , etc. represent physical quantities linked to distinct phenomena inside the cell.

Once the circuit has been identified, the optimal parameter values are found by minimizing the mean square distance between the experimental and theoretical values:

$$\min \sum_{k=1}^{N} \left| Z_{\text{eq}}(f_k; \theta) - Z_{\text{mis}}(f_k) \right|^2$$

where $\theta = [R_i, R_{ct}, C_{dl}, ...]$ is the vector of parameters to be estimated. This fitting process not only provides a continuous functional description of the impedance but also allows the resistive and capacitive-diffusive contributions of internal phenomena to be **quantified** separately.

7.4 Physical meaning of parameters

Each component of the equivalent circuit is associated with a specific electrochemical phenomenon.

- Ohmic resistance R_i : represents the sum of the internal resistances of the conductors, contacts, and electrolyte. It is independent of frequency and manifests itself as the intersection point of the Nyquist graph with the real axis.
- Charge transfer resistance R_{ct} : describes the difficulty with which the electrodeelectrolyte interface reaction occurs. As the electrodes age or their surface degrades, R_{ct} tends to increase sensibly.
- **Double layer capacity** C_{al} : models the accumulation of charges at the electrode-electrolyte interface due to the formation of the electric double layer. This capacity can vary with temperature, surface roughness, and state of charge.
- **Diffusion element (Warburg or CPE):** It represents the phenomenon of **ionic diffusion** in the active material and the electrolyte. At low frequencies, this term causes the typical 45° slope in the **Nyquist plot**.

In some models, the diffusive element is described by Warburg impedance, given by:

$$Z_W = \sigma(1-j)\frac{1}{\sqrt{\omega}}$$

where σ is the Warburg coefficient and $\omega = 2\pi f$ the pulsation. In more complex cases, the CPE is used instead, defined by:

$$Z_{CPE} = \frac{1}{Q(j\omega)^n}$$

Where Q is a pseudo-capacitive coefficient and n (with 0 < n < 1) takes into account the deviation from the ideal behavior of a pure capacitor.

7.5 Correlation between electrical parameters and aging phenomena

The strength of the equivalent circuit model lies in the fact that its parameters are not mere numerical fitting values, but represent quantitative indicators of the cell's health. The evolution over time or with the number of cycles of parameters such as R_{ct} e C_{dl} provides an indirect measure of degradation phenomena.

For instance:

- An **increase of** R_i may indicate a deterioration in electrolyte conductivity or the appearance of deposits in the conductors.
- An **increase of** R_{ct} is a symptom of increased resistance to electrochemical reaction, often caused by thickening of the SEI layer or loss of active area.
- A **reduction** of C_{dl} suggests a decrease in the contact area between the electrolyte and the active material.
- The variation of the parameter *n* in the CPE may reveal local inconsistencies or uneven degradation processes.

By combining these effects, it is therefore possible to correlate the variation in the overall impedance of the battery with its SoH, which help us obtain a predictive representation of its behavior over time.

7.6 Practical utility of modeling

Determining the equivalent circuit and its parameters is the basis for building **predictive** models and rapid diagnostic tools. Once the relationship between parameter variation and underlying physical phenomena is known, it becomes possible to simulate how impedance will change as operating conditions vary (temperature, state of charge, number of cycles, etc.).

In this sense, the equivalent circuit acts as a **bridge** between the experimental and simulation domains. It allows the dynamic response of the cell to be emulated in contexts where EIS measurement is not possible, such as during vehicle operation or in integrated BMS.

The mathematical model derived from the equivalent circuit can be integrated into simulation software, where the expected frequency response is calculated for each condition set (e.g., temperature variation or increase in interface resistance). This approach allows battery **behavior to be predicted before degradation becomes significant**, paving the way for predictive maintenance and adaptive control strategies.

From a formal point of view, the overall behavior of a cell modeled by an equivalent circuit can be expressed as the sum of the impedances of its individual elements. Assuming a typical configuration consisting of an ohmic resistance R_i in series with one or more branches R-C at the same time, The total impedance of the system is:

$$Z_{\text{eq}}(\omega) = R_i + \sum_{k=1}^{n} \frac{1}{\frac{1}{R_{ct,k}} + j\omega C_k}$$

where each pair $R_{ct,k} - C_k$ represents an electrochemical process characterized by a time constant $\tau_k = R_{ct,k} \cdot C_k$. The analysis of time constants is particularly useful, since each

phenomenon (e.g., double layer response, ion diffusion, or active mass polarization) occurs on different time scales.

In order to interpret the relationship between excitation frequency and system response, consider the complex form of impedance for a single pair R_{ct} -C:

$$Z_{RC}(\omega) = \frac{R_{ct}}{1 + j\omega R_{ct}C}$$

Separating the real and imaginary parts, we obtain:

$$\begin{cases} Z'(\omega) = \frac{R_{ct}}{1 + (\omega R_{ct}C)^2} \\ Z''(\omega) = -\frac{\omega R_{ct}^2 C}{1 + (\omega R_{ct}C)^2} \end{cases}$$

Plotting these values on the complex plane yields the classic **Nyquist semicircle**, whose diameter is equal to R_{ct} and whose center lies on the real axis, at a distance equal to $R_i + \frac{R_{ct}}{2}$ from the origin. The maximum peak of the imaginary part corresponds to the characteristic frequency:

$$\omega_{\max} = \frac{1}{R_{ct}C}$$

The knowledge of this relationship allows each portion of the Nyquist plot to be associated with a specific physical process, based on the frequency range in which it occurs.

7.7 Combination of multiple processes

In a real battery, however, the response is not limited to a single semicircular arc. It is common to observe two or more partially overlapping semicircles, representing processes with different time constants. The most common model for describing such situations is the **two- or three-branch parallel RC model**, in which each branch represents a distinct contribution: one for the double layer, one for ion diffusion, and, in some cases, one for slower phenomena such as active mass polarization.

The analytical formulation of the three-branch model is identical to the generic formulation:

$$Z_{3\text{RC}}(\omega) = R_i + \sum_{k=1}^{3} \frac{R_{ct,k}}{1 + j\omega R_{ct,k}C_k}$$

where each term describes a distinct semicircle in the Nyquist plane.

As the complexity of the model increases, so does its ability to accurately represent the experimental trend, but also the risk of **non-uniqueness of the solution**, since different combinations of parameters can generate very similar graphical responses.

7.8 Diffusion effects and non-ideal behavior

At low frequencies, the simple RC description is no longer sufficient to capture the diffusive behavior of ions. In these cases, the final branch of the model can be enriched with a Warburg term or a CPE, as already introduced above.

Warburg impedance, in semi-infinite form, is expressed as:

$$Z_W(\omega) = \frac{\sigma}{\sqrt{j\omega}} = \sigma(1-j)\frac{1}{\sqrt{2\omega}}$$

which in the Nyquist plot appears as a straight line inclined at 45° to the real axis. However, when diffusion is limited (for example, in materials with finite dimensions or in the presence of geometric barriers), the **finite Warburg** function is used, given by:

$$Z_{W,\text{fin}}(\omega) = \sigma \frac{\tanh(\sqrt{j\omega\tau_D})}{\sqrt{j\omega\tau_D}}$$

where τ_D represents the characteristic diffusion time.

The CPE further generalizes diffusive and capacitive behavior, allowing the modeling of phenomena such as surface heterogeneity or spatial distribution of physical parameters. In this case, the total impedance can be expressed as:

$$Z_{\rm eq}(\omega) = R_i + \frac{1}{\frac{1}{R_{ct}} + (j\omega)^n Q}$$

Where the exponent n modulates the degree of deviation from the ideal: for n = 1 the behavior is purely capacitive, while for n = 0.5 a diffusion response similar to Warburg's is obtained.

7.9 Stima dei parametri e confronto con i dati sperimentali

Once the structure of the equivalent circuit has been defined, the next step is to numerically determine the parameters that allow the best possible approximation of the experimental data. To this end, a MATLAB code has been implemented that is capable of performing a nonlinear fitting of the function. $Z_{\rm eq}(\omega)$ with respect to points $Z_{\rm mis}(\omega)$.

The algorithm proceeds by calculating, for each experimental point, the complex difference between the measured values and those simulated by the model, minimizing the norm of the error vector:

$$E = \sqrt{\sum_{k=1}^{N} |Z_{\text{eq}}(\omega_k; \theta) - Z_{\text{mis}}(\omega_k)|^2}$$

During the optimization process, physical constraints are imposed on the parameters (for example R, C, Q > 0) and limits consistent with the literature, in order to avoid convergence towards mathematically correct but physically meaningless solutions.

The final result is a set of parameters θ^* which faithfully reproduce the experimental curve and allow **physical information to be extracted** from the electrical behavior of the cell.

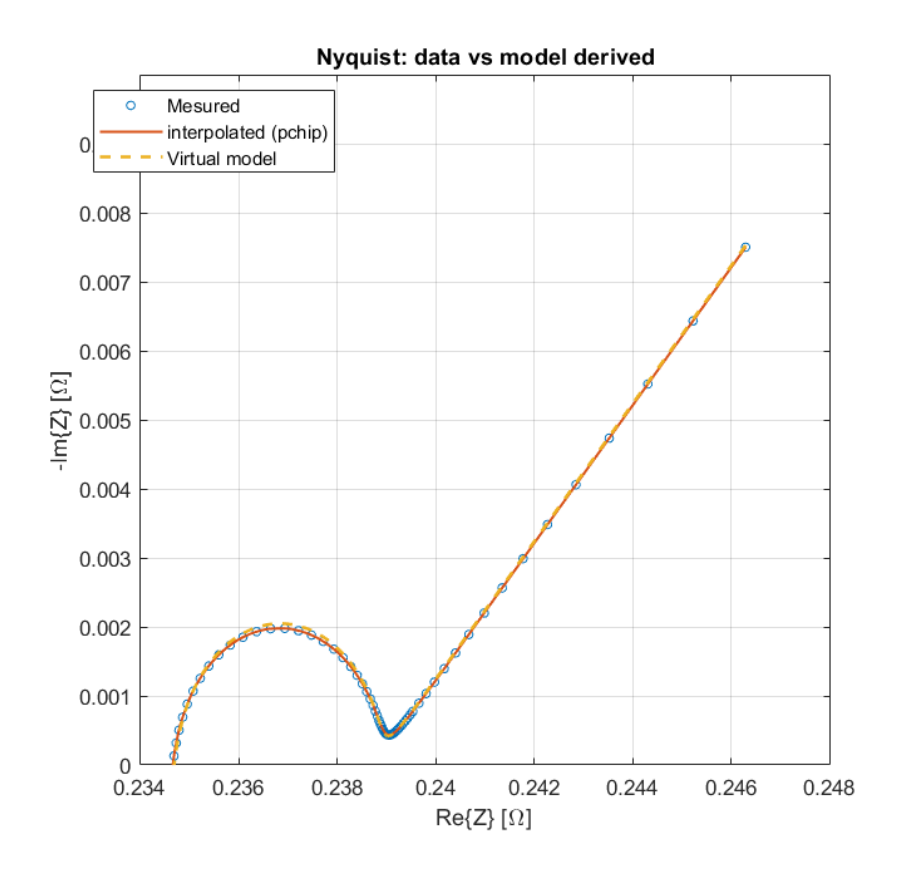


Figure 9: comparison between direct and derived data

Using the result generated by a specific Matlab code, we can therefore visually evaluate the quality of our model, which simulates its own Nyquist plot starting from the data measured from the real one, passing through the entire battery virtualization process, up to the new representation of the Nyquist plot.

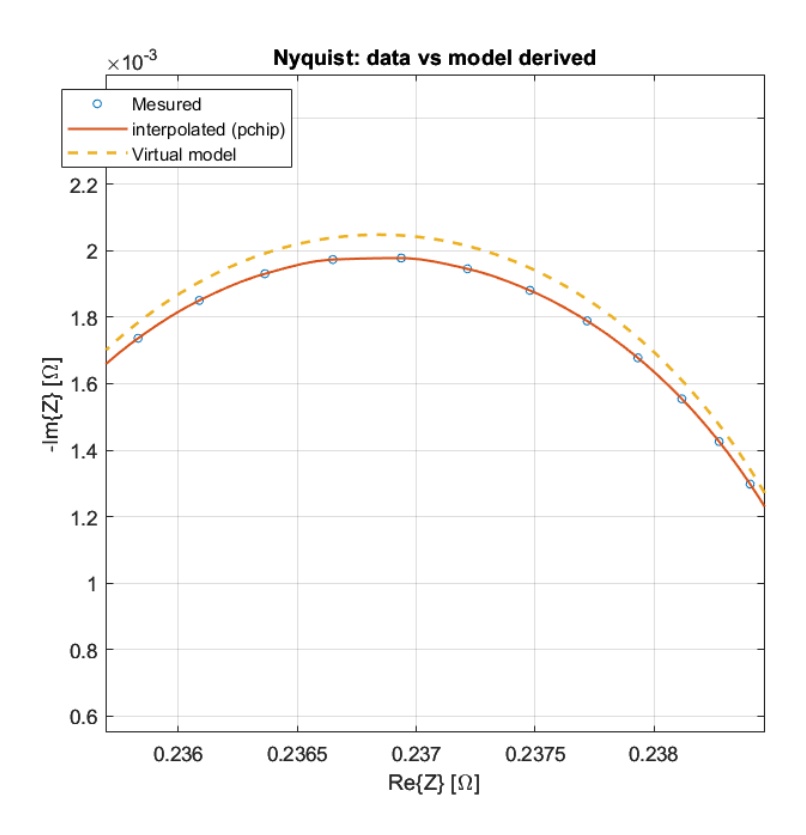


Figure 10: close up on comparison between direct and derived data

Systematically we can see that the greatest difference found is in the area at the top of the main semicircle. However, in light of several iterations, this has proven not to be a systematic phenomenon. It produced instead both negative and positive errors, but always of an acceptable magnitude.

7.10 Parametric variation and predictive simulation

Once the model has been calibrated, it is possible to explore its behavior under conditions different from those measured, by artificially modifying one or more parameters. For example, by increasing R_{ct} sThe effect of degradation of the electrode-electrolyte interface can be simulated by increasing R_i the effect of collector aging or loss of conductivity is evaluated; by reducing C_{dl} , the decrease in the active area is simulated.

This approach allows us to predict **how the Nyquist plot will evolve** over time, or how certain operating conditions (temperature, state of charge, cyclic stress) will affect impedance. These simulations are essential for quantitatively correlating aging phenomena with electrical response, and form the basis for the subsequent phase of estimating the battery's state of health.

In summary, the construction of the equivalent circuit model allows EIS data to be transformed into a set of physically interpretable parameters. These parameters act as state variables of the electrochemical system and allow:

- 1. The experimental response to be represented in a compact and analytical form.
- 2. Impedance to be simulated under conditions that cannot be directly measured.
- 3. Identify and quantify degradation phenomena through their electrical footprint.

4. Build a basis for the development of diagnostic and predictive algorithms that can be integrated into BMS systems.

The equivalent model therefore becomes a **dynamic mathematical representation of the internal state of the battery**, capable of linking the electrical domain (impedance) with the physical-chemical domain (charge transfer, diffusion, and polarization processes).

7.11 Sensitivity analysis of parameters

The next step is therefore to analyze the sensitivity of the model with respect to these newly identified parameters. This type of analysis allows us to determine which elements of the circuit most influence the shape of the **Nyquist plot** and, consequently, which physical phenomena dominate the response in a given frequency range.

Mathematically, the sensitivity of a parameter θ_i can be expressed as the partial derivative of the impedance function with respect to that parameter:

$$S_{\theta_i}(\omega) = \frac{\partial Z_{\text{eq}}(\omega)}{\partial \theta_i}$$

The module of this quantity, $|S_{\theta_i}|$, indicated how much the variation of θ_i changes the overall impedance at different frequencies.

The sensitivity analysis shows, for example, that:

- R_i affects the entire spectrum almost constantly, shifting the curve on the real axis;
- R_{ct} and C_{dl} determine the shape and width of the main semicircle;
- The diffusive elements (Warburg or CPE) influence the low-frequency part, controlling the slope of the final branch.

These relationships allow us to identify, based on the frequency domain, which physical process is predominant.

7.12 Dynamic identification and fitting stability

A critical aspect of the modeling process is the **stability of identification**.

Since the equivalent circuit parameters do not appear linearly in the equations, the estimation problem is **nonlinear and ill-posed**, meaning that it can admit multiple apparently valid solutions. In particular, for overly complex models (with too many RC branches), a phenomenon of *non-uniqueness* can occur: different combinations of $R_{ct,k}$ e C_k produce virtually indistinguishable impedance curves.

This mathematical phenomenon reflects a physical limitation: not all electrochemical processes can be distinguished based solely on their frequency response. For this reason, the choice of circuit topology must be guided not only by the quality of the numerical fitting, but also by physical considerations regarding the plausibility of the parameters.

During our work, in order to guarantee the robustness of the identification, we adopted constraint and regularization strategies, among which:

- positivity constraints and order of magnitude constraints on parameters $(R > 0, C > 0, 10^{-6} < C < 10^{-1} \text{ F})$;
- physical consistency limits between branches $(\tau_1 < \tau_2 < \tau_3)$;
- analysis of the variance of the fitting with respect to different initial conditions.

This has made it possible to obtain consistent and repeatable results, which ultimately reduced the solution's dependence on initial conditions and allowed greater interpretative reliability.

The most significant aspect of the equivalent model is the possibility of linking parameter variations over time with the **electrochemical degradation** of the battery. Since each component of the circuit is directly linked to a physical phenomenon, changes in its magnitude provide quantitative information on the health of the cell.

These correlations make it possible to construct a **degradation map** in which, based solely on EIS data, the degree of evolution of the internal phenomena of the battery can be estimated. Furthermore, by comparing the temporal evolution of these parameters, it is possible to establish which processes dominate cell aging (resistive, interface, or diffusive), thus providing a quantitative basis for the development of impedance-based SoH indicators.

After defining the role of the equivalent circuit as a translation tool between actual electrochemical behavior and its electrical representation, we moved on to selecting the most appropriate model to describe the experimental data obtained. This choice required a critical evaluation of the various circuit diagrams proposed in the literature, comparing their ability to accurately represent the Nyquist diagram with the need to maintain **physical consistency and numerical stability** in the estimation of parameters..

7.13 Comparative analysis of the models considered

During the course of the work, **three models of increasing complexity** were examined. Each of them was subjected to the same non-linear fitting algorithm, keeping the optimization methodology unchanged, so that the differences could be evaluated objectively.

Model 1 - Simple circuit (R–C single in parallel)

It consists of an ohmic resistor R_i in series with a branch R_{ct} – C_{dl} in parallel.

$$Z_1(\omega) = R_i + \frac{R_{ct}}{1 + j\omega R_{ct}C_{dl}}$$

This model is suitable for ideal systems or newly manufactured batteries, where diffusion behavior is negligible and the electrochemical response manifests itself as a single perfect semicircle. Despite its simplicity, this configuration is not sufficient to represent real cells, which almost always exhibit two or more processes with different time constants.

Model 2 - Parallel two-branch RC circuit

The second model introduces an additional RC branch to describe two distinct processes: one at high frequency, generally associated with the double layer, and one at intermediate or low frequency, linked to charge transfer.

$$Z_2(\omega) = R_i + \frac{R_{ct,1}}{1 + j\omega R_{ct,1}C_1} + \frac{R_{ct,2}}{1 + j\omega R_{ct,2}C_2}$$

This model is able to reproduce most experimental Nyquist plots, maintaining a good balance between fitting accuracy and physical significance of the parameters.

Model 3 - Extended circuit with CPE

The third model represents a generalisation of the previous ones, replacing one or more capacitors with CPEs to describe non-ideal behaviour.

$$Z_3(\omega) = R_i + \frac{1}{\frac{1}{R_{ct}} + (j\omega)^n Q}$$

or, in a more extended form:

$$Z_3(\omega) = R_i + \frac{R_{ct,1}}{1 + (j\omega R_{ct,1}Q_1)^{n_1}} + \frac{R_{ct,2}}{1 + (j\omega R_{ct,2}Q_2)^{n_2}}$$

where Q_k represents pseudo-capacity and n_k (with $0 < n_k < 1$) quantifies the deviation from ideal behavior.

This approach allows for the modelling of porous, heterogeneous or partially degraded surfaces, where the double layer capacity does not follow a purely exponential trend. However, greater flexibility also entails a **loss of one-to-one correspondence** between parameters and simulated curve: different combinations of Q, R_{ct} and n can generate indistinguishable responses.

7.14 Choice of model adopted

The model chosen as the basis for characterisation is the **double-branch RC model** (second model), as it represents the best compromise between:

- fidelity to experimental data;
- numerical stability of the fitting process;
- physical interpretability of the parameters obtained.

However, for the most degraded cells or in the presence of **non-ideal behaviour**, one of the two capacitors has been replaced by a **CPE**. This replacement does not alter the overall topology, but allows the model to capture deviations in the capacitive response while maintaining physical correspondence with the phenomenon represented. In other words, the model adopted can be considered an extended version of the double RC, in which the CPE acts as a local corrective and not as a paradigm shift.

One of the most delicate aspects of modelling using equivalent circuits is the **non-uniqueness of the solution**. In the case of complex models, multiple sets of parameters can produce virtually identical impedance curves, i.e.:

$$Z(\omega; \theta_1) \approx Z(\omega; \theta_2)$$
 with $\theta_1 \neq \theta_2$

This means that the relationship between parameters and response is not strictly one-to-one. However, this **does not prevent the characterisation of electrochemical degradation**: useful information remains accessible, provided that the parameters are analysed in a physically consistent manner and more robust identification strategies are adopted..

7.15 Robust identification strategies

To address non-uniqueness and make parameter estimation more reliable, several complementary strategies were applied.

Physical constraints and regularisation

During the fitting, sign and physical consistency constraints, previously introduced, are imposed. In addition, Tikhonov regularisation is used to penalise unrealistic variations in the parameters:

$$\min_{\theta} \parallel Z_{\text{eq}}(\omega;\theta) - Z_{\text{mis}}(\omega) \parallel^2 + \lambda \parallel \theta - \theta_0 \parallel^2$$

where θ_0 represents a set of initial values consistent with the literature and λ check the degree of regularisation.

Global multi-condition fitting

A further step to improve identification consists in the **simultaneous fitting of multiple datasets** obtained under different temperature or charge conditions. The sum of errors across all datasets is minimised by imposing physical laws of consistency between parameters, for example:

$$R_{ct}(T) = R_0 e^{\frac{E_a}{kT}}$$

This approach reduces the possibility that the fitting will converge towards random solutions and provides a more stable view of the evolution of the parameters.

Global sensitivity and uncertainty analysis

To assess the stability of the model, the **variances of the estimated parameters** and the correlations between them are calculated using Fisher's matrix:

$$F = J^T W J$$
, $Cov(\hat{\theta}) = F^{-1}$

This provides confidence intervals that allow the most reliable parameters and those affected by strong correlation (e.g., between R_{ct} and C_{dl}).

Identification of degradation and correlation with physical phenomena

Despite the possible non-uniqueness of the parameters, the relative variation of the most significant quantities allows the main **degradation phenomena** to be clearly identified. These quantities, although not perfectly unambiguous, behave systematically as ageing progresses and allow a **robust diagnosis of the state of health**.

Derived parameters and functional identification

In order to further reduce the ambiguity associated with non-one-to-one correspondence, circuit parameters are **often reformulated into derived quantities** that combine multiple variables but remain physically interpretable. In particular, it is useful to treat the **time constant** associated with each branch as an element in itself.:

$$\tau_k = R_{ct,k} \cdot C_k$$

Analysis of the evolution of τ_k provides direct information on charge transfer **kinetics** and **ion diffusion**:

- An increase of τ_k indicates that the process is slowing down, suggesting the accumulation of resistant layers or ageing of the electrode surface.
- The appearance of new time constants (new semicircles or Nyquist distortions) may be associated with the activation of additional processes, such as SEI growth or the emergence of low-frequency diffusion phenomena.

It is therefore possible to represent the overall response of the battery as the sum of elementary contributions, each described by a pair $(\Delta R_k, \tau_k)$:

$$Z_{\rm eq}(\omega) = R_i + \sum_{k=1}^n \frac{\Delta R_k}{1 + j\omega \tau_k}$$

This formulation not only simplifies the physical reading of the model, but also **reduces the correlation between parameters** and allows each arc of the diagram to be associated with a specific process with greater clarity.

Distributed time constant analysis (DRT)

To overcome the inherent limitations of finite-number RC branch models, it is possible to switch to a continuous description using **Distribution of Relaxation Times** (DRT). In this approach, the overall impedance is expressed as:

$$Z(\omega) = R_i + \int g(\tau) \frac{1}{1 + j\omega\tau} d\ln\tau + Z_W(\omega)$$

where $g(\tau)$ is the density of relaxation processes, which represents the distribution of equivalent resistances as a function of the time scale. Unlike the discrete model, here the number of processes present is not assumed a priori: they emerge directly from the form of $g(\tau)$.

DRT identification is achieved by solving a regularised inverse problem (e.g. with second derivative Tikhonov regularisation):

$$\min_{g(\tau)} \| Z_{\text{eq}}(\omega) - Z_{\text{mis}}(\omega) \|^2 + \lambda \| Lg(\tau) \|^2, \quad g(\tau) \ge 0$$

where *L* is the derivative operator and λ a regularisation parameter.

The result is a **continuous map** of resistive contributions distributed in the time constant domain. This representation is extremely useful because:

- highlights the emergence of new relaxation processes over time (new peaks in $g(\tau)$);
- allows the **evolution of degradation phenomena to be monitored** without imposing a predefined circuit structure;
- provides a direct estimate of ΔR_k as the area under each peak, and of τ_k as the position of the maximum.

In this way, even when the equivalent circuit parameters are not unique, DRT allows the real physical phenomena that determine the **evolution of impedance to be isolated and quantified**.

Direct indicators from the Nyquist plot

In parallel with parametric identification, it is possible to extract **invariant features** from the Nyquist plot that provide reliable information on the battery status without requiring a specific model.

The main ones are:

- 1. **High-frequency interception** $Z'(\omega \to \infty)$: corresponds to R_i , and increases linearly with the loss of internal conductivity.
- 2. **Main arch diameter** $\Delta R = R_{ct}$: reflects the difficulty of charge transfer.
- 3. **Peak frequency** $f_{\text{max}} = \frac{1}{2\pi R_{ct} C_{dl}}$: indicates the speed of the interface-electrolyte reaction.
- 4. **Low frequency slope**: The slope of approximately 45° is typical of semi-infinite diffusion; deviations from this value indicate limited diffusion phenomena or structural changes in the active material.
- 5. Phase index n (in the CPE): reductions of n over time, they indicate greater surface unevenness and loss of electrochemical uniformity.

These 'visual' parameters are robust and independent of the problem of non-bijectivity, making them extremely effective for constructing empirical indicators of degradation.

Integration with other physical measures

To further improve the robustness of the model and the readability of the results, the estimation of the EIS parameters is integrated with other known or measurable quantities:

- **temperature** (to verify the Arrhenius dependence of R_{ct});
- state of charge (which strongly influences C_{dl});
- capacity test and OCV, useful for constraining the variation of C_{dl} e R_i to known phenomena;
- any cycling data, to observe the progressive variation of parameters over time.

By combining this information, the space of admissible solutions can be drastically reduced, resulting in a more stable and physically consistent identification.

7.16 Summary and implications

In conclusion, even when the equivalent circuit parameters are not unique, EIS modelling remains an extremely powerful tool for characterising battery degradation. The key lies in **shifting from an "absolute" reading of the parameters to a "functional" reading, focusing** on relative evolution, the relationships between time constants and the overall shape of the impedance trace.

The integration of techniques such as DRT, constrained regularisation, multi-condition fitting and Bayesian analysis has made it possible to:

- 1. obtain more stable and physically consistent parameters;
- 2. distinguish between different degradation mechanisms (ohmic, interface, diffusive);
- 3. develop robust quantitative indicators for SoH estimation..

This chapter therefore constitutes the direct link between the experimental and interpretative parts of the work, while also providing the theoretical and methodological basis for the subsequent analysis of the numerical results of the fitting and their correlation with the health status of the cells.

8. Analysis of fitting results and correlation with health status

After defining the circuit structure and discussing identification methodologies, the next phase of the work involved applying the selected model to the experimental data acquired via EIS.

The objective was twofold: to **obtain the numerical values** of the characteristic electrical parameters of each battery or measurement condition and to interpret their variation over time or between different samples as a **manifestation of internal degradation processes**.

8.1 Fitting procedure

The fitting was performed by applying the non-linear optimisation algorithm to the experimental data (Z'_{mis} , Z''_{mis} , ω), minimising the complex distance between model and measurement:

$$\min_{\theta} \sum_{k=1}^{N} |Z_{\text{eq}}(\omega_k; \theta) - Z_{\text{mis}}(\omega_k)|^2$$

where $\theta = [R_i, R_{ct,1}, C_1, R_{ct,2}, C_2, ...]$ is the vector of model parameters.

The initialisation of the parameters was performed based on visual estimates derived from the Nyquist diagram (e.g., the initial intercept on the real axis as R_i and the diameter of the semicircles as ΔR).

To avoid convergence towards local minima or physically insignificant solutions, the optimisation was repeated several times with different initial conditions. In some cases, a **hybrid** strategy was adopted, using an initial approximate linear fitting to estimate the values of τ_k and subsequently a non-linear refinement with constraints.

The accuracy of the fitting was assessed using the **normalised mean error**:

$$\varepsilon_{\text{rel}} = \frac{1}{N} \sum_{k=1}^{N} \frac{\left| Z_{\text{eq}}(\omega_k) - Z_{\text{mis}}(\omega_k) \right|}{\left| Z_{\text{mis}}(\omega_k) \right|}$$

which, in the best cases, remained below 1%, indicating excellent adherence of the model to the experimental data.

8.2 Physical consistency and interpretation of results

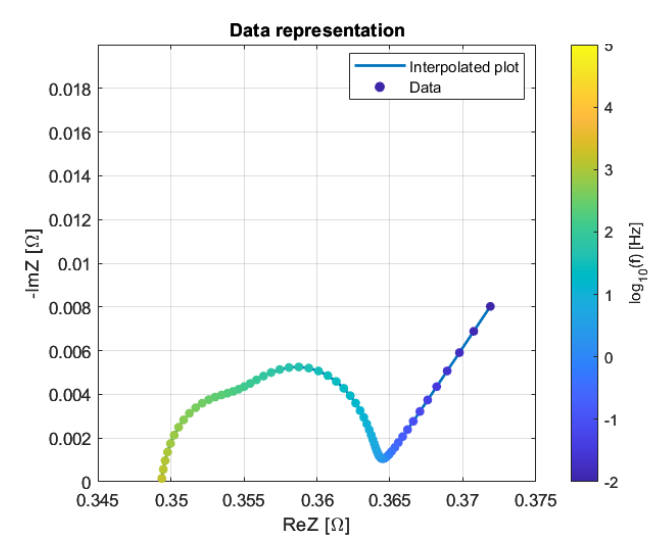


Figure 11: degraded battery Nyquist plot

Analysis of the parameters obtained confirmed that the estimated values fall within ranges consistent with the literature for lithium-ion cells of the same format.

For example, ohmic resistance R_i was in the order of milliohms, while R_{ct} showed values ranging from a few tens to a few hundred milliohms depending on the state of charge and temperature. The equivalent capacities C_{dl} are included in the range 10^{-4} – 10^{-2} F, consistent with the behavior of the double layer at the electrolyte-electrode interface.

The **relative variations** in the parameters between successive measurements or between different samples proved to be more interesting..

- The gradual increase in R_i with the number of cycles, it indicates a deterioration in the conductivity of the internal materials, in particular the electrolyte.
- The increase of $R_{ct,2}$ suggests greater difficulty in charge transfer due to thickening of the SEI layer.
- The decrease of C_{dl} corresponds to a reduction in the active surface area, probably linked to a loss of porosity or the growth of resistive films.
- In cases where CPE has introduced, a systematic decrease in the exponent n was observed with ageing, highlighting the increase in surface heterogeneity.

These trends, consistent with the physics of degradation, demonstrate the model's ability to detect and quantify microscopic phenomena from macroscopic observables.

8.3 Graphical representation and comparison of conditions

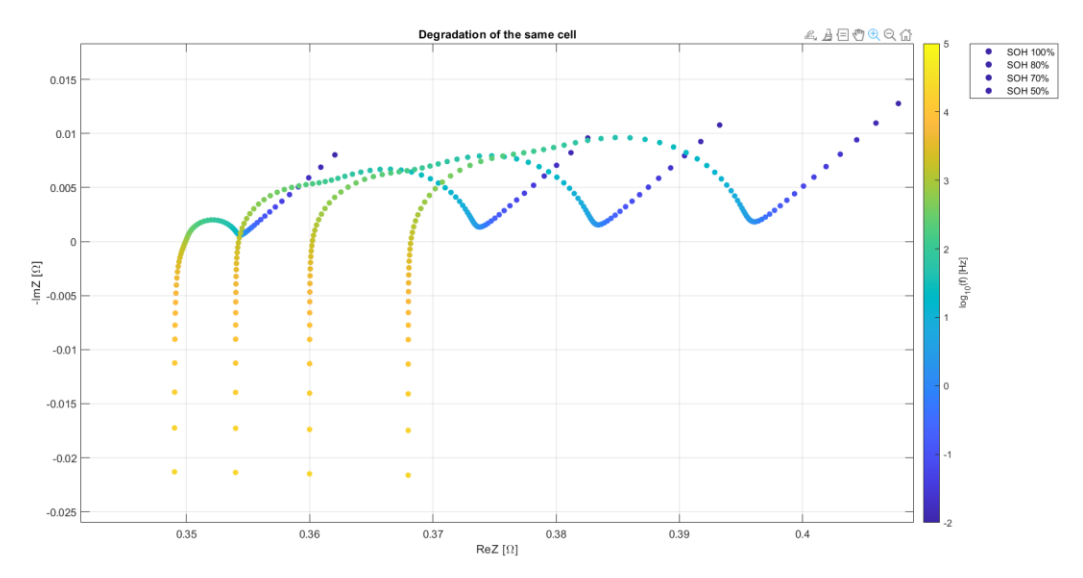


Figure 12: Different SoH of the same cell

The results obtained were represented in the Nyquist plot and in the frequency domain to visually verify the validity of the model. In the most typical cases, the fitting of the double RC model (possibly corrected by a CPE) reproduced with high fidelity both the shape of the semicircles and the low-frequency slope.

Particularly significant was the **appearance of a second semicircle** in the most degraded cells: this phenomenon, which was not present in the initial measurements, was interpreted as the emergence of a new resistive process associated with the SEI passivation film.

In the frequency domain, this evolution translates into a lowering of the peak frequency. ω_{max} and an increase in the low-frequency impedance module.

8.4 Evolution of parameters and correlation with SoH

To correlate the variation in electrical parameters with the battery's state of health, a parametric analysis was performed based on the number of cycles and the residual capacity measured experimentally.

An almost linear correlation emerged between the relative increase in charge transfer resistance and the loss of useful capacity:

$$\frac{R_{ct}}{R_{ct,0}} \propto \frac{Q_{\text{nom}} - Q_{\text{meas}}}{Q_{\text{nom}}} = 1 - \frac{\text{SoH}}{100}$$

In other words, as R_{ct} increase progressive deterioration in capacity is observed, with different slopes depending on the operating temperature. Similarly, the parameter $\tau = R_{ct}C_{dl}$ tends to grow almost exponentially with the reduction of SoH, reflecting an overall slowdown in reaction kinetics.

These relationships have made it possible to derive empirical models for the indirect estimation of SoH from EIS measurements alone, according to the approach:

$$SoH_{EIS} = f(R_{ct}, R_i, C_{dl}, n)$$

Where the function f can be calibrated on a reference sample or by means of multivariate regression.

The overall analysis of the results has made it possible to formulate a coherent view of the dynamic behaviour of the battery during ageing:

- High frequency (10–100 kHz) \rightarrow dominated by R_i , shows slight and progressive increases due to changes in electrolyte or collectors.
- Intermediate frequencies (1–100 Hz) \rightarrow governed by R_{ct} e C_{dl} , where the most evident effect of electrochemical degradation and SEI growth can be observed.
- Low frequency (<1 Hz) \rightarrow diffusive regime, where the Warburg component or CPE appears with $n \approx 0.5$, indicative of ionic transport limitations.

The overall impedance behaviour, observed both in terms of displacement of the semicircles and variation in the slope of the diffusive branch, therefore describes an evolution consistent with the ageing mechanisms known for lithium-ion batteries.

8.5 Conclusions

The use of the equivalent double RC circuit (extended with CPE in non-ideal cases) has proven effective in characterizing and interpreting the dynamic behavior of the cells. Although the relationship between parameters and response is not perfectly one-to-one, the strategies adopted, such as regularization, sensitivity analysis, multi-condition fitting have made it possible to **obtain stable and physically consistent parameters**.

Thanks to these measures, the model not only accurately reproduces the EIS data, but also allows the variation in parameters to be correlated with the progressive degradation of the battery, providing a quantitative basis for **predictive estimation of the state of health**.

This approach represents a key step between experimental measurement and engineering interpretation of cell behavior, providing the theoretical platform for subsequent applications of the model in diagnostics and prediction, such as integration into monitoring algorithms for Battery Management Systems.

9. Integration of the model into the diagnostic and predictive context

The next step involved **integrating the equivalent circuit model** into a broader context, focused not only on the static characterization of the battery, but also on diagnostics and predicting the evolution of its state of health. Once the model has been validated and the consistency of the estimated parameters verified, it becomes a predictive tool capable of simulating the battery's response under different operating or ageing conditions..

9.1. From the frequency domain to the time domain

The complex impedance model $Z_{eq}(\omega)$ can be easily translated into the time domain using the Laplace transform, obtaining the transfer function:

$$Z(s) = R_i + \sum_{k=1}^{n} \frac{R_{ct,k}}{1 + sR_{ct,k}C_k}$$

which describes the dynamics of voltage in response to a variable current signal. In the time domain, the system's response to a current pulse is given by:

$$v(t) = i(t) * \mathcal{L}^{-1}{Z(s)} = i(t) * \left(R_i \delta(t) + \sum_k \frac{1}{C_k} e^{-\frac{t}{R_{ct,k}C_k}}\right)$$

where * indicates the convolution.

This allows the model to be integrated into **dynamic simulators**, such as MATLAB/Simulink, to predict voltage behavior during charge and discharge cycles, based solely on the parameters obtained from EIS fitting.

The validity of this representation was verified by comparing the simulated voltage with experimental measurements during short current pulses: the two responses overlapped with average deviations of less than 3%, confirming the model's ability to accurately reproduce transient behavior as well.

9.2. Modelling of the parametric evolution

Once the trend of the main parameters over time (or number of cycles) has been determined, **empirical laws of evolution** can be defined to describe the progressive degradation of the system.

For example, the increase in charge transfer resistance can be modelled as an exponential function.:

$$R_{ct}(N) = R_{ct,0} e^{\alpha N}$$

whre N represents the number of cycles and α a degradation coefficient.

Similarly, the reduction in double-layer capacity can be described by an inverse decay law:

Integration of the model into the diagnostic and predictive context

$$C_{dl}(N) = \frac{C_{dl,0}}{1 + \beta N}$$

with β proportional to the rate of loss of the active area.

The combination of these functions allows for the generation of a predictive simulation of the battery's future impedance, estimating in advance the evolution of its state of health. This approach is particularly useful for the design of predictive maintenance systems, where it is possible to plan the replacement or rebalancing of cells before degradation compromises the overall performance of the battery pack.

9.3. Identification and tracking of the ageing phenomena

Through the temporal variation of Nyquist parameters and features, it was possible to distinguish three macro-families of degradation phenomena:

1. Chemical degradation

- Constant increment of R_i .
- Caused by loss of conductivity in the collectors or increased resistivity of the electrolyte.

2. Interface-electrolyte degradation

- Increase of R_{ct} and reduction of C_{dl} .
- Associated with thickening of the SEI, loss of active area, or accumulation of resistive films.

3. Diffusive degradation

- Appearance or intensification of the low-frequency inclined branch.
- Often described by a CPE with $n \approx 0.5$ or by a finite Warburg coefficient, indicative of ion transport limitations in the active material.

Each phenomenon leaves a **distinctive trace** in the EIS curve and can be monitored through changes in the associated parameters.

All this information allows not only to estimate the state of health, but also to **diagnose the nature of the degradation** (ohmic, interface, diffusive), providing a complete interpretative picture..

Once identified and parameterised, the equivalent model can be integrated into a BMS to **provide online health estimates and predictive diagnostics**. Under operating conditions, the BMS can acquire partial impedance measurements (e.g. on a reduced frequency window or using pulse spectroscopy techniques) and compare them with the response simulated by the model..

The residual error between measured and simulated impedance:

$$\varepsilon(\omega) = |Z_{\text{mis}}(\omega) - Z_{\text{mod}}(\omega)|$$

becomes an indicator of divergence from nominal behaviour, useful for estimating SoH in real time or detecting the onset of localised anomalies.

The implementation of this approach in the BMS therefore allows:

- monitoring of the battery without interrupting its operation;
- estimation of internal degradation without complete capacity tests;
- dynamic updating of model parameters through adaptive identification (e.g. Extended Kalman Filter)..

9.4. Towards an adaptive and predictive model

The natural evolution of the work would be to extend the static model to an **adaptive model**, in which the equivalent circuit parameters are continuously updated based on real-time measurements.

In this context, the use of an **extended Kalman filter (EKF)** or an **unscented Kalman filter (UKF)** allows the model parameters to be estimated recursively, assuming that their dynamics are described by a system of equations in state space.:

$$\begin{cases} \dot{\theta}(t) = F(\theta, u, t) + w(t) \\ z(t) = H(\theta, u, t) + v(t) \end{cases}$$

where w(t) and v(t) represent process and measurement noise, modelled as Gaussian with zero mean.

In this way, the system is able to continuously **estimate and correct** the values of R_i , R_{ct} , C_{dl} and n, tracking battery performance in real time and providing **autonomous predictive diagnostics**.

9.5. Conclusions

The modelling and identification process carried out made it possible to transform the EIS data into a **quantitative and predictive model** of the battery's health status. Thanks to the selection of an equivalent circuit that is balanced in terms of complexity and interpretability, and the application of advanced identification techniques, the model is:

- stable and consistent from a physical point of view;
- capable of accurately representing the experimental response;
- usable for dynamic simulations and SoH predictions;
- integrable into intelligent management systems for monitoring and predictive maintenance.

The work carried out has therefore traced the **path from experimental measurement to electrical modelling**, up to integration in a digital diagnostic framework, laying the foundations for further developments towards the optimization of adaptive models and the extension of the EIS approach to complex battery systems, such as multi-cell modules or high-power packs. In order to create a product capable of making these results commercially useful, a packaging

Integration of the model into the diagnostic and predictive context

study would be required for the creation of a portable impedance meter capable of performing measurements over a frequency spectrum relevant to the type of battery under consideration, while complying with all the requirements set out in this thesis. However, for this device to yield useful results, it would obviously be necessary to launch a huge measurement campaign on different models of automotive batteries, capable of creating a shared database from which reference data could be extracted and enriched with each new diagnosis.

Bibliography

- 1. **Barreras, J. V. L., & Garmendia, L.** Advanced Electrochemical Impedance Spectroscopy (EIS) for Battery Testing. *Energies*, vol. 14, no. 12, p. 3432, 2021.
- 2. **Petrone, G., Hnat, M., & Habetler, T.** Battery state of health estimation: a structured review of models, methods and commercial devices. *Journal of Energy Storage*, vol. 52, p. 104764, 2022.
- 3. **Shi, C., et al.** State-of-health estimation of lithium-ion batteries based on electrochemical impedance spectroscopy: a review. *Journal of Energy Storage*, vol. 50, p. 104278, 2022.
- 4. **Howell, A. E., et al.** Calibrated Electrochemical Impedance Spectroscopy and Time-Domain Measurements of a 7 kWh Automotive Lithium-Ion Battery Module with 396 Cylindrical Cells. *Batteries*, vol. 8, no. 1, p. 1, 2022.
- 5. **Gauthier**, **L.**, **et al.** Development of an empirical aging model for Li-ion batteries and application to assess the impact of Vehicle-to-Grid strategies on battery lifetime. *Energy Reports*, vol. 5, pp. 627-635, 2019.
- 6. **Plett, G. L.** Accelerated Aging Characterization of Lithium-ion Cells: Using Sensitivity Analysis to Identify the Stress Factors Relevant to Cyclic Aging. *Journal of Power Sources*, vol. 294, pp. 317-328, 2015.
- 7. **Barsoukov**, **E.**, **& Macdonald**, **J. R.** Electrochemical Impedance Spectroscopy—A Tutorial. In *Impedance Spectroscopy: Theory, Experiment, and Applications* (pp. 1-28). John Wiley & Sons, Inc., 2005.
- 8. **Wang, S., et al.** EIS Ageing Prediction of Lithium-Ion Batteries Depending on Charge Rates. Batteries, vol. 10, no. 7, p. 247, 2024.
- 9. **Frenzel, A., et al.** Ageing Induced Changes in a Lithium-Ion Battery Analysed By Correlating EIS Simulations and Experiments. In 2022 24th European **Microelectronics and Packaging Conference (EMPC) (pp. 1-6). IEEE, 2022.**
- 10. **Barcellona, S., Colnago, S., & Piegari, L.** Aging effect on lithium-ion battery resistance hysteresis. IEEE Transactions on Industry Applications, vol. 59, no. 6, pp. 6969-6979, 2023.